
When predict can also explain: few-shot prediction to select better neural latents

Kabir Dabholkar¹ Omri Barak²

Abstract

Latent variable models serve as powerful tools to infer underlying dynamics from observed neural activity. Ideally, the inferred dynamics should align with true ones. However, due to the absence of ground truth data, prediction benchmarks are often employed as proxies. One widely-used method, *co-smoothing*, involves jointly estimating latent variables and predicting observations along held-out channels to assess model performance. In this study, we reveal the limitations of the co-smoothing prediction framework and propose a remedy. In a student-teacher setup with Hidden Markov Models, we demonstrate that the high co-smoothing model space encompasses models with arbitrary extraneous dynamics in their latent representations. To address this, we introduce a secondary metric — *few-shot co-smoothing*, performing regression from the latent variables to held-out channels in the data using fewer trials. Our results indicate that among models with near-optimal co-smoothing, those with extraneous dynamics underperform in the few-shot co-smoothing compared to ‘minimal’ models that are devoid of such dynamics. We provide analytical insights into the origin of this phenomenon and further validate our findings on real neural data using two state-of-the-art methods: LFADS and STNDT. In the absence of ground truth, we suggest a novel measure to validate our approach. By cross-decoding the latent variables of all model pairs with high co-smoothing, we identify models with minimal extraneous dynamics. We find a correlation between few-shot co-smoothing performance and this new measure. In summary, we present a novel prediction metric designed to yield latent variables that more accurately reflect the ground truth, offer-

ing a significant improvement for latent dynamics inference. [Code available here.](#)

1. Introduction

In neuroscience, we often have access to simultaneously recorded neurons during certain behaviors. These observations, denoted \mathbf{X} , offer a window onto the actual hidden (or latent) dynamics of the relevant brain circuit, denoted \mathbf{Z} (Vyas et al., 2020). Although, in general, these dynamics can be complex and high-dimensional, capturing them in a concrete mathematical model opens doors to reverse-engineering, revealing simpler explanations and insights (Barak, 2017; Sussillo & Barak, 2013). Inferring a model of the \mathbf{Z} variables, also known as latent variable modeling (LVM), is part of the larger field of system identification with applications in many areas outside of neuroscience, such as fluid dynamics (Vinueza & Brunton, 2022) and finance (Bauwens & Veredas, 2004).

Because we don’t have ground truth for \mathbf{Z} , prediction metrics on held-out parts of x are commonly used as a proxy (Pei et al., 2021). However, it has been noted that prediction and explanation are often distinct endeavors (Shmueli, 2010). For instance, (Versteeg et al., 2023) use an example where ground truth is available to show how different models that all achieve good prediction nevertheless have varied latents that can differ from the ground truth. Such behavior might be expected when using highly expressive models with large latent spaces. Bad prediction with good latents is demonstrated by (Koppe et al., 2019) for the case of chaotic dynamics.

Various regularisation methods on the latents have been suggested to improve the similarity of \mathbf{Z} to the ground truth, such as recurrence and priors on external inputs (Pandarinath et al., 2018), low-dimensionality of trajectories (Sedler et al., 2022), low-rank connectivity (Valente et al., 2022; Pals et al., 2024), injectivity constraints from latent to predictions (Versteeg et al., 2023), low-tangling (Perkins et al., 2023), and piecewise-linear dynamics (Koppe et al., 2019). However, the field lacks a quantitative, *prediction-based* metric that credits the simplicity of the latent representation—an aspect essential for interpretability and ultimately scientific discovery, while still enabling comparisons across a wide range of LVM architectures.

¹Faculty of Mathematics

Technion - Israel Institute of Technology, Haifa, Israel ²Rappaport Faculty of Medicine and Network Biology Research Laboratory, Technion - Israel Institute of Technology, Haifa, Israel. Correspondence to: Kabir Dabholkar <kabir@campus.technion.ac.il>, Omri Barak <omri.barak@gmail.com>.

Here, we characterize the diversity of model latents achieving high *co-smoothing*, a standard prediction-based framework for Neural LVMs, and demonstrate potential pitfalls of this framework. We propose a few-shot variant of co-smoothing which, when used in conjunction with co-smoothing, differentiates varying latents. We verify this approach both on synthetic toy problems and state-of-the-art methods on neural data, providing an analytical explanation of why it works in a simple setting.

2. Related Work

Our work builds on recent developments in Neural LVMs for the discovery of latent structure in noisy neural data on single trials. We refer the reader to (Pei et al., 2021) supplementary table 3 for a comprehensive list of Neural LVMs published from 2008-2021. Central to our work is the co-smoothing procedure, which evaluates models based on the prediction of activity from held-out neurons provided held-in neuron activity from the same trial. Co-smoothing was first introduced in (Yu et al., 2008) and (Macke et al., 2011) for the validation of GPFA as a Neural LVM.

(Pei et al., 2021) curated four datasets of neural activity recorded from behaving monkeys and established a framework to evaluate co-smoothing among other prediction-based metrics on several models in the form of a standardized benchmark and competition.

In contrast to prediction approaches, a parallel line of work focuses on explaining and validating Neural LVMs on synthetic data, enabling direct comparison with the ground truth (Sedler et al., 2022; Brenner et al., 2022; Durstewitz et al., 2023). (Versteeg et al., 2023) validated their method with both ground truth and neural data, demonstrating high predictive performance with low-dimensional latents.

A concept we introduce is cross-decoding across a population of models to find the most parsimonious representation. Several works compare representations of large model populations (Maheswaranathan et al., 2019; Morcos et al., 2018). They apply Canonical Correlation Analysis (CCA), a symmetric measure of representational similarity, whereas we use regression, which is not symmetric. The application to Neural LVMs may be novel.

One related approach comparing representations in deep neural networks is *stitching* components of separately trained (and subsequently frozen) models into a composite model using a simple linear layer (Lenc & Vedaldi, 2015; Bansal et al., 2021).

Central to our work is the concept of few-shot learning a decoder from a frozen intermediate representation. (Sorscher et al., 2022) developed a theory of geometric properties of representations that enables few-shot generalization to novel

classes. They identified the geometric properties that determine a signal-to-noise ratio for classification, which dictates few-shot performance. While this setting differs from ours, links between our works are a topic for future research. To our knowledge, the use of few-shot generalization as a means to identify interpretable latent representations, particularly for Neural LVMs, is a novel idea.

3. Co-smoothing: a cross-validation framework

Let $\mathbf{X} \in \mathbb{Z}_{\geq 0}^{T \times N}$ be spiking neural activity of N channels recorded over a finite window of time, i.e., a *trial*, and subsequently quantised into T time-bins. $X_{t,n}$ represents the number of spikes in channel n during time-bin t . The dataset $\mathcal{X} := \{\mathbf{X}^{(i)}\}_{i=1}^S$, partitioned as $\mathcal{X}^{\text{train}}$ and $\mathcal{X}^{\text{test}}$, consists of S trials of the experiment. The latent-variable model (LVM) approach posits that each time-point in the data $\mathbf{X}_{t,:}^{(i)}$ is a noisy measurement of a latent state $\mathbf{Z}_{t,:}^{(i)}$.

To infer the latent trajectory \mathbf{Z} is to learn a mapping $f : \mathbf{X} \mapsto \mathbf{Z}$. On what basis do we validate the inferred \mathbf{Z} ? We have no ground truth on \mathbf{Z} , so instead we test the ability of \mathbf{Z} to predict unseen or held-out data. Data may be held-out in time, e.g., predicting future data points from the past, or in space, e.g., predicting neural activities of one set of neurons (or channels) based on those of another set. The latter is called co-smoothing (Pei et al., 2021).

The set of N available channels is partitioned into two: N^{in} held-in channels and N^{out} held-out channels. The S trials are partitioned into train and test. During training, both channel partitions are available to the model and during test, only the held-in partition is available. During evaluation, the model must generate the $T \times N^{\text{out}}$ rate-predictions $\mathbf{R}_{\cdot,\text{out}}$ for the held-out partition. This framework is visualised in Fig. 1A.

Importantly, the encoding-step or inference of the latents is done using a full time-window, i.e., analogous to *smoothing* in control-theoretic literature, whereas the decoding step, mapping the latents to predictions of the data is done on individual time-steps:

$$\mathbf{Z}_{t,:} = f(\mathbf{X}_{\cdot,\text{in}}; t) \quad (1)$$

$$\mathbf{R}_{t,\text{out}} = g(\mathbf{Z}_{t,:}), \quad (2)$$

where the subscripts ‘in’ and ‘out’ denote partitions of the neurons. During evaluation, the held-out data from test trials $\mathbf{X}_{\cdot,\text{out}}$ is compared to the rate-predictions $\mathbf{R}_{\cdot,\text{out}}$ from the model using the co-smoothing metric \mathcal{Q} defined as the

normalised log-likelihood, given by:

$$Q(R_{t,n}, X_{t,n}) := \frac{1}{\mu_n \log 2} \left(\mathcal{L}(R_{t,n}; X_{t,n}) - \mathcal{L}(\bar{r}_n; X_{t,n}) \right) \quad (3)$$

$$\mathcal{Q}^{\text{test}} := \sum_{n \in \text{held-out}} \sum_{i \in \text{test}} \sum_{t=1}^T Q(R_{t,n}^{(i)}, X_{t,n}^{(i)}), \quad (4)$$

where \mathcal{L} is poisson log-likelihood, $\bar{r}_n = \frac{1}{TS} \sum_i \sum_t X_{t,n}^{(i)}$ is the mean rate for channel n , and $\mu_n := \sum_i \sum_t X_{t,n}^{(i)}$ is the total number of spikes, following (Pei et al., 2021).

Thus, the inference of LVM parameters is performed through the optimization:

$$f^*, g^* = \operatorname{argmax}_{f,g} \mathcal{Q}^{\text{train}} \quad (5)$$

using $\mathcal{X}^{\text{train}}$, without access to the test trials from $\mathcal{X}^{\text{test}}$. For clarity, apart from equation 5, we report only $\mathcal{Q}^{\text{test}}$, omitting the superscript.

4. Good co-smoothing does not guarantee correct latents

It is common to assume that being able to predict held-out parts of \mathbf{X} will guarantee that the inferred latent aligns with the true one (Macke et al., 2011; Pei et al., 2021; Wu et al., 2018; Meghanath et al., 2023; Keshtkaran et al., 2022; Keeley et al., 2020; Le & Shlizerman, 2022; She & Wu, 2020; Wu et al., 2017; Zhao & Park, 2017; Schimel et al., 2022; Mullen et al., 2024; Gokcen et al., 2022; Yu et al., 2008; Perkins et al., 2023). To test this assumption, we use a student-teacher scenario where we know the ground truth. To compare how two models (u, v) align, we infer the latents of both from $\mathcal{X}^{\text{test}}$, then do a regression from latents of u to v . The regression error is denoted $\mathcal{D}_{u \rightarrow v}$ (i.e. $\mathcal{D}_{T \rightarrow S}$ for teacher to student decoding). Contrary to the above assumption, we hypothesize that good prediction guarantees that the true latents are contained within the inferred ones (low $\mathcal{D}_{S \rightarrow T}$), but not vice versa (Fig. 1C). It is possible that the inferred latents possess additional features, unexplained by the true latents (high $\mathcal{D}_{T \rightarrow S}$).

To verify this hypothesis, we choose both student and teacher to be discrete-space, discrete-time Hidden Markov Models (HMMs). As a teacher model, they simulate two important properties of neural time-series data: its dynamical nature and its stochasticity. As a student model, they are perhaps the simplest LVM for time-series, yet they are expressive enough to capture real neural dynamics¹. Please see appendix A for a further discussion on the choice of

model class. In Appendix E we replicate our analyses in linear gaussian state space models. The HMM has a state space $z \in \{1, 2, \dots, M\}$, and produces observations (emissions in HMM notation) along neurons \mathbf{X} , with a state transition matrix \mathbf{A} , emission model \mathbf{B} and initial state distribution π . More explicitly:

$$\begin{aligned} A_{m,l} &= p(z_{t+1} = l | z_t = m) & \forall m, l \\ B_{m,n} &= p(x_{n,t} = 1 | z_t = m) & \forall m, n \\ \pi_m &= p(z_0 = m) & \forall m \end{aligned} \quad (6)$$

The same HMM can serve two roles: a) data-generation by sampling from equation 6 and b) inference of the latents from data on a trial-by-trial basis:

$$\xi_{t,m}^{(i)} = f_m((\mathbf{X}_{:,in})^{(i)}) = p(z_t^{(i)} = m | (\mathbf{X}_{:,in})^{(i)}), \quad (7)$$

i.e., *smoothing*, computed exactly with the forward-backward algorithm (Barber, 2012). Note that although z is the latent state of the HMM, we use its posterior probability mass function ξ_t as the relevant intermediate representation. To make predictions of the rates of held-out neurons for co-smoothing we compute:

$$R_{n,t}^{(i)} = g_n(\xi_t^{(i)}) = \sum_m B_{m,n} \xi_{t,m}^{(i)}. \quad (8)$$

As a teacher, we constructed a 4-state model of a noisy chain $A_{m,l} \propto \mathbb{I}[l = (m + 1) \bmod M] + \epsilon$, with $\epsilon = 1e - 2$, $\pi = \frac{1}{M}$, and $B_{m,n} \sim \text{Unif}(0, 1)$ sampled once and frozen (Fig. 2, left). We generated a dataset of observations from this teacher (see appendix I). We trained 400 students with 4 – 15 states on the same teacher data using gradient-based methods (see appendix B). All students had high co-smoothing scores, with some variance, and a trend for large students to perform better. Consistent with our hypothesis, the ability to decode the teacher from the student varied little, and was highly correlated to the co-smoothing score (Fig. 1D). In contrast, the ability to decode the student from the teacher displayed a large variability, and little correlation to the co-smoothing score (Fig. 1E). See appendix C for details of the regression.

What is it about a student model, that produces good co-smoothing with the wrong latents? We consider the HMM transition matrix for the teacher and two exemplar students – named “Good” and “Bad” (marked by green and red arrows in Fig. 1CD) – and visualise their states and transitions using graphs in Fig. 2. The teacher is a cycle of 4 steps. The good student also contains such a cycle (orange), and the initial distribution π is restricted to that cycle, rendering the other states irrelevant. In contrast, the *bad* student also contains this cycle (orange), but the π distribution is not consistent with the cycle leading to an extraneous branch converging to the cycle, as well as a departure from the

¹ \mathcal{Q} of 0.29 for HMMs vs. 0.24 for GPFA and 0.35 for LFADS, on mc_maze_20

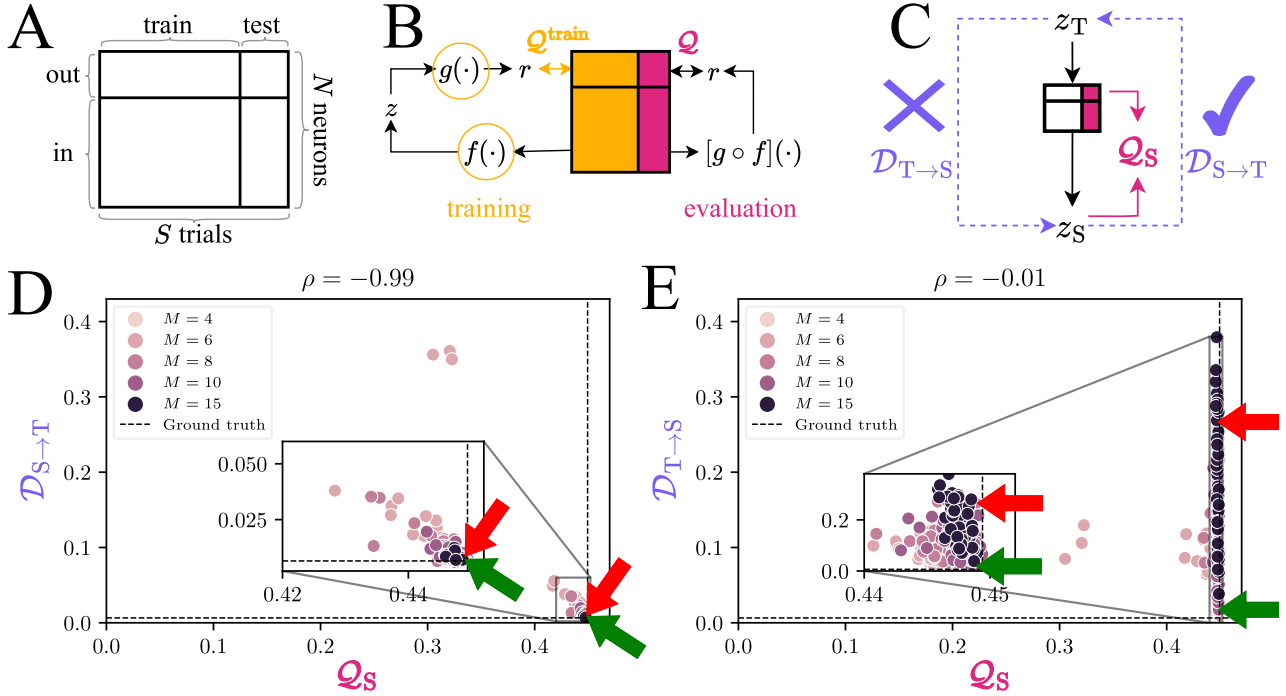


Figure 1. Prediction framework and its relation to ground truth. **A.** To evaluate a neural LVM with co-smoothing, the dataset is partitioned along the neurons and trials axes. **B.** The held-in neurons are used to infer latents z , while the held-out serve as targets for evaluation. The encoder f and decoder g are trained jointly to maximise co-smoothing Q . After training, the composite mapping $g \circ f$ is evaluated on the test set. **C.** We hypothesise that models with high co-smoothing may have an asymmetric relationship to the true system, ensuring that model representation contains the ground truth, but not vice-versa. We reveal this in a synthetic student(S)-teacher(T) setting by the unequal performance of regression on the states in the two directions. $\mathcal{D}_{u \rightarrow v}$ denote decoding error of model v latents z_v from model u latents z_u . **D.** Several student HMMs are trained on a dataset generated by a single teacher HMM. The Student \rightarrow Teacher decoding error $\mathcal{D}_{S \rightarrow T}$ is low and tightly related to the co-smoothing score. **E.** The Teacher \rightarrow Student decoding error $\mathcal{D}_{T \rightarrow S}$ is more varied and uncorrelated to co-smoothing. Dashed lines represent the ground truth, evaluating the teacher itself as a candidate model. A score of $Q = 0$ corresponds to predicting the mean firing-rate for each neuron at all trials and time points. Green and red arrows represent “Good” and “Bad” models respectively, presented in Fig. 2.

main cycle (both components in dark colour). Note that this does not interfere with co-smoothing, because the emission probabilities $B_{m,n}$ of the extra states are consistent with true states, i.e., the emission matrix conceals the extraneous dynamics.

5. Few-shot prediction selects better models

Because our objective is to obtain latent models that are close to the ground truth, the co-smoothing prediction scores described above are not satisfactory. Can we devise a new prediction score that will be correlated with ground truth similarity? The advantage of prediction benchmarks is that they can be optimized, and serve as a common language for the community as a whole to produce better algorithms (Deng et al., 2009).

We suggest **few-shot co-smoothing** as a complementary prediction score to co-smoothing, to be used on models

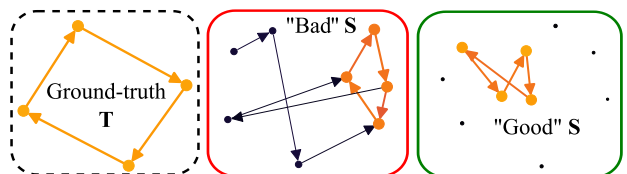


Figure 2. Visualisations of HMMs: the ground truth T along with two representative extreme student models. Circles represent states, and arrows represent transitions. Circle area and edge widths, reflect fraction of visitations or volume of traffic after sampling the HMM over several trials, each trial, a sequence of T time steps. The colours also reflect the same quantity – brighter for higher traffic. Edges with values below 0.02 are removed for clarity. The teacher ($M = 4$) is a 4-cycle. Note the prominent 4-cycles (orange) present in the good student ($M = 10$), and the bad student ($M = 8$). In the good student, the extra states are seldom visited, whereas in the bad student there is significant extraneous dynamics involving these states (dark arrows).

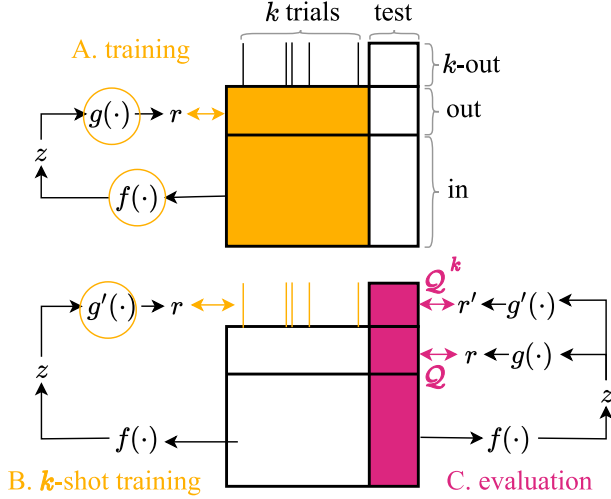


Figure 3. Co-smoothing and few-shot co-smoothing; a composite evaluation framework for Neural LVMs. **A.** The encoder f and decoder g are trained jointly using held-in and held-out neurons. **B.** A separate decoder g' is trained to readout k -out neurons using only k trials. Meanwhile, f and g are frozen. **C.** The neural LVM is evaluated on the test set resulting in two scores: co-smoothing Q and k -shot co-smoothing Q^k .

with good scores on the latter. Similarly to standard co-smoothing, the functions g and f are trained using all trials of the training data (Fig. 3A). The key difference is that a separate group of $N^{k\text{-out}}$ neurons is set aside, and only k trials of these neurons are used to estimate a mapping $g' : Z_{t,:} \mapsto R_{t,k\text{-out}}$ (Fig. 3B), similar to g in equation 2. The neural LVM (f, g, g') is then evaluated on both the standard co-smoothing Q using $g \circ f$ and the few-shot version Q^k using $g' \circ f$ (Fig. 3C).

This procedure may be repeated several (s) times independently on resampled sets of k trials, giving s estimates of g' , each yielding a score Q^k for each k -set. For small k , the Q^k s tend to be highly variable. Thus we compute and report the average score $\langle Q_S^k \rangle$ over the s resamples for each student S . Practical advice on how to choose the value of k and s is given in appendix H.

To show the utility of the newly-proposed prediction score, we return to the same HMM students from Fig. 1. For each student, we evaluate $\langle Q_S^k \rangle$. This involves estimating the bernoulli emission parameters $\hat{B}_{m,k\text{-out}}$, given the latents $\xi_{t,m}^{(i)}$ using equation 42 and then generating rate predictions for the k -out neurons using equation 8. First, we see that it provides new information on the models, as it is not correlated with standard co-smoothing (Fig. 4A). We also show that it is not simply a harder version of co-smoothing (appendix D). We are only interested in models that have good co-smoothing, and thus select students sat-

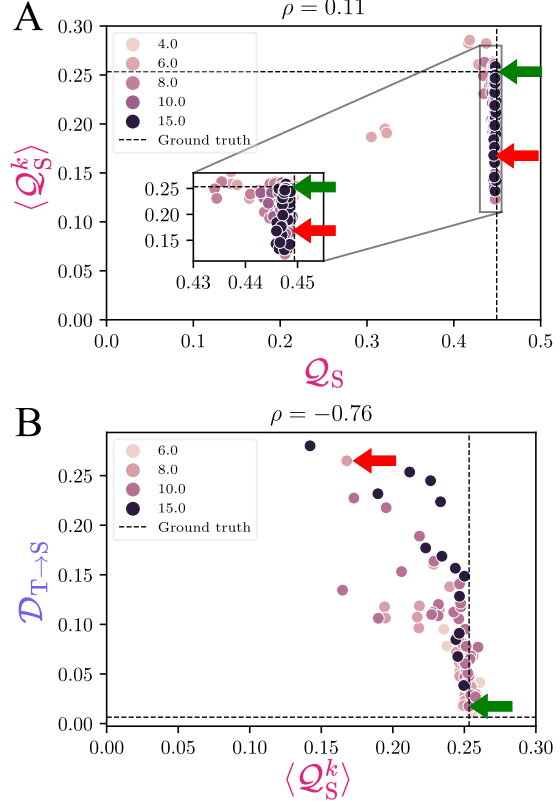


Figure 4. Few-shot prediction selects better models. **A.** Student models with high co-smoothing have highly variable 6-shot co-smoothing and uncorrelated to co-smoothing. **B.** For the set of students with high co-smoothing, i.e., satisfying $Q_S > Q_T - 10^{-3}$, 6-shot co-smoothing to held-out neurons is negatively correlated with decoding error from teacher-to-student. Following Fig. 4C,D dashed lines represent the ground truth, green and red arrows represent “Good” and “Bad” models (Fig. 2).

isfying $Q_S > Q_T - \epsilon$, choosing $\epsilon = 10^{-3}$. For these students, we see that despite having very similar co-smoothing scores, their k -shot scores $\langle Q_S^k \rangle$ are highly correlated with the ground truth measure $D_{T \rightarrow S}$ (Fig. 4B). Taken together, these results suggest that the combined objective of maximising Q_S and $\langle Q_S^k \rangle$ simultaneously – both prediction based objectives – yields models achieving low $D_{S \rightarrow T}$ and $D_{T \rightarrow S}$, a more complete notion of model similarity to the ground truth.

6. Why does few-shot work?

The example HMM students of Fig. 2 can help us understand why few-shot prediction identifies good models. The students differ in that the *bad* student has more than one state corresponding to the same teacher state. Because these states provide the same output, this feature does not hurt co-smoothing. In the few-shot setting, however, the output

of all states needs to be estimated using a limited amount of data. Thus the information from the same amount of observations has to be distributed across more states. We make this data efficiency argument more precise in three settings: HMMs, linear regression and prototype learning.

Consider a student-teacher scenario as in section 4. We let $T = 2$ and use a stationary teacher $z_1^{(i)} = z_2^{(i)}$. Now consider two examples of inferred students. To ensure a fair comparison, we use two latent states for both students. In the *good* student, ξ , these two states statistically do not depend on time, and therefore it does not have extraneous dynamics. In contrast, the *bad* student, μ , uses one state for the first time step, and the other for the second time step. A particular example of such students is:

$$\xi_t = [0.5 \quad 0.5]^T \quad t \in \{1, 2\} \quad (9)$$

$$\mu_{t=1} = [1 \quad 0]^T \quad \mu_{t=2} = [0 \quad 1]^T \quad (10)$$

where each vector corresponds to the two states, and we only consider two time steps.

We can now evaluate the maximum likelihood estimator of the emission matrix \hat{B} from k trials for both students, and compare it to the teacher B^* . In the case of bernoulli HMMs the maximum likelihood estimate of g' given a fixed f and k trials has a closed form. For a single output neuron, it is:

$$\begin{aligned} \hat{B}(\xi) &= \frac{0.5(C_1+C_2)}{0.5kT} & \hat{B}_1(\mu) &= \frac{C_1}{k} \\ \hat{B}_2(\xi) &= \frac{0.5(C_1+C_2)}{0.5kT} & \hat{B}_2(\mu) &= \frac{C_2}{k} \end{aligned} \quad (11)$$

where C_t is the number of times $x = 1$ at time t in k trials. We see that C_t is a sum of k i.i.d. Bernoulli random variables (RVs) with the teacher parameter B^* , for both $t = 1, 2$. We see that for both students \hat{B} are unbiased, but the bad student's \hat{B} has higher variance.

Using a Taylor expansion of the loss around the teacher emission matrix (appendix N), we obtain:

$$\mathbb{E}_{\hat{B}_k} L_\xi \left(\hat{B}_k(\xi) \right) \approx L(B^*) - \frac{1}{2k}, \quad (12)$$

$$\mathbb{E}_{\hat{B}_k} L_\mu \left(\hat{B}_k(\mu) \right) \approx L(B^*) - \frac{1}{k}. \quad (13)$$

Thus, the good teacher ξ has a better performance for low k .

We can construct a similar scenario for linear regression, with continuous latents (appendix L). The latents have a signal dimension and several noise dimensions, corresponding to the extraneous dynamics. In this case, the variance does not discriminate between students, but the bias does – still leading to higher error for extraneous dynamics in low k . Crucially, if k larger than a critical value, the effect vanishes.

Finally, we use prototype learning for binary classification on continuous latents (appendix M). Here too, we show that variance underlies the ability of low k to discriminate models. In this setting, however, the effect gradually diminishes with k .

7. SOTA LVMS on neural data

In section 4 we showed that models with near perfect co-smoothing may possess latents with extraneous dynamics. We established this in a synthetic student-teacher setting with simple HMM models.

To show the applicability in more realistic scenarios, we trained several models from two SOTA architectures, LFADS (Sedler & Pandarinath, 2023; Pandarinath et al., 2018; Keshtkaran et al., 2022), a variational autoencoder (Kingma, 2013), and STNDT (Le & Shlizerman, 2022; Ye & Pandarinath, 2021), a transformer (Nguyen & Salazar, 2019; Huang et al., 2020), on `mc_maze_20` consisting of neural activity recorded from monkeys performing a maze solving task (Churchland et al., 2010), curated by (Pei et al., 2021). The 20 indicates that spikes were binned into 20ms time bins. We evaluate co-smoothing on a test set of trials and define the set of models with the best co-smoothing (appendix F and I).

An integral part of LFADS and STNDT training is the random hyperparameter sweep which generates several candidate solutions to the optimization problem equation 5.

With each model f_u , we infer latents evaluated over a fixed set of test trials $\mathcal{X}^{\text{test}}$, using equation 1.

In the HMM case, we had ground truth that enabled us to directly compare the student latent to that of the teacher. With real neural data we do not have this privilege. To nevertheless reveal the presence or absence of extraneous dynamics, we instead compare the models to each other. The key idea is that all models contain the teacher latent, because they have good co-smoothing. One can then imagine that each student contains a selection of several extraneous features. The best student is the one containing the least such features, which would imply that all other students can decode its latents, while it cannot decode theirs. We therefore use *cross-decoding* among student models as a proxy to the ground truth.

Instead of computing $\mathcal{D}_{S \rightarrow T}$ and $\mathcal{D}_{T \rightarrow S}$ as in section 4 we perform cross-decoding from latents of model u to model v ($\mathcal{D}_{u \rightarrow v}$) for every pair of models u and v using linear regression and evaluating an R^2 score for each mapping (appendix F). In Fig. 19 the results are visualised by a $U \times U$ matrix with entries $\mathcal{D}_{u \rightarrow v}$ for all pairs of models u and v .

We hypothesize that the latents z_u contain the information

necessary to output good rate predictions r that match the outputs plus the arbitrary extraneous dynamics. This former component must be shared across all models with high \mathcal{Q} , whereas the latter could be unique in each model – or less likely to be consistent in the population. The ideal model v^* would have no extraneous dynamics therefore, all the other models should be able to decode to it with no error, i.e., $\mathcal{D}_{u \rightarrow v^*} = 0 \forall u$. Provided a large and diverse population of models only the ‘pure’ ground truth would satisfy this condition. To evaluate how close is a model v to the ideal v^* we propose a simple metric: the column average $\langle \mathcal{D}_{u \rightarrow v} \rangle_u$. This will serve as proxy for the distance to ground truth, analogous to $\mathcal{D}_{T \rightarrow S}$ in Fig. 4. We validate this procedure using the student-teacher HMMs in appendix G, where we show it is highly correlated to ground truth, and as correlated to few-shot as the SOTA models.

Having developed a proxy for the ground truth we can now correlate it with the few-shot regression to held-out neurons. Fig. 6 shows a negative correlation for both architectures, similar to the HMM examples above. As an illustration of the latents of different models, Fig. 19 shows the PCA projection of several trials from two different models. Both have high co-smoothing scores (LFADS: 0.3647, 0.3643, STNDT: 0.3488, 0.3495), but differ in their cross-decoding column average $\langle \mathcal{D}_{u \rightarrow v} \rangle_u$. Note the somewhat smoother trajectories in the model with higher few-shot score. It is also possible to cross-decode across the two populations, as shown in Appendix K.

8. Discussion

Latent variable models aim to infer the underlying latents using observations of a target system. We showed that co-smoothing, a common prediction measure of the goodness of such models cannot discriminate between certain classes of latents. In particular, extraneous dynamics can be invisible to such a measure.

We suggest a complementary prediction measure: few-shot co-smoothing. Instead of directly regressing from held-in to held-out neurons as is done to evaluate co-smoothing, we distinguish the encoder and the decoder. To evaluate the trained model we substitute the decoder with a new decoder estimated using only a ‘few’ (k) number of trials. The rate predictions provided by the few-shot decoder are evaluated the same as in standard co-smoothing. Using synthetic datasets and HMM models, we show numerically and analytically that this measure correlates with the distance of model latents to the ground truth.

We demonstrate the applicability of this measure to real world neural datasets, with SOTA architectures. This required developing a new proxy to ground truth – cross decoding. For each pair of SOTA models that we obtained, we

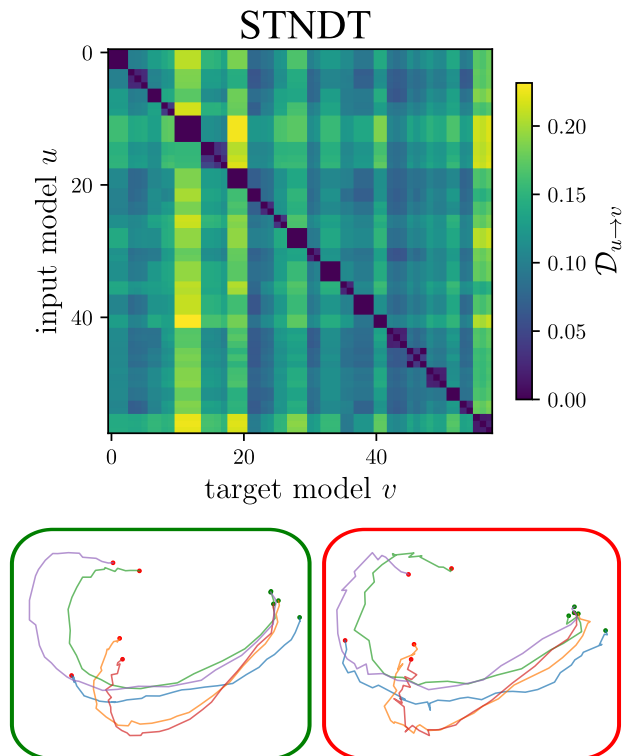


Figure 5. Cross-decoding as a proxy for distance to the ground truth in near-SOTA models. 120 STNDT models were trained on the `mc_maze_20` dataset then selected for high-cosmoothing (appendix F). **Top:** The latents of each pair of models were decoded from one another, and the decoding error is shown in the matrices. Good models are expected to be decoded from all other models, and hence have low values in their corresponding columns. **Bottom:** Trajectories of two STNDT models, with the lowest (left and in the green box, best model:= $\text{argmin}_v \langle \mathcal{D}_{u \rightarrow v} \rangle_u$) and highest (right and in the red box, the worst model:= $\text{argmax}_v \langle \mathcal{D}_{u \rightarrow v} \rangle_u$) column averaged cross-decoding errors, projected onto their leading two principal components. Scores for these models are indicated in Fig. 6 by the arrows. Each trace is the trajectory for a single trial, starting at a green dot and ending at a red dot. The same analysis was performed on LFADS models (appendix O).

performed a linear regression across model latents, provided identical input data. Models with extraneous dynamics showed up as a bad target latent on average, and vice versa. Finally we show that these two characterisations of extraneous dynamics are correlated. An interesting extension would be to use this new metric as another method to select good models. The computational cost is high, because it requires training a population of models and comparing between all of them. It is also less universal and standardised than few-shot co-smoothing, as it is dependent on a specific ‘jury’ of models. The HMM results, however, show that it is more correlated to ground truth than the few-shot.

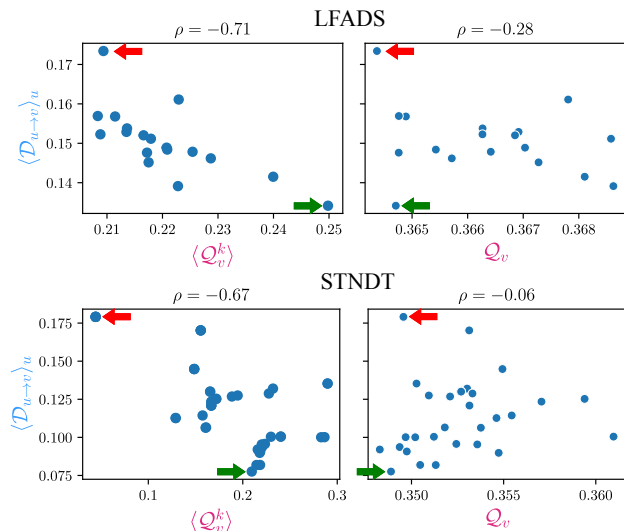


Figure 6. Few-shot scores correlate with the proxy of distance to the ground truth. Several models of two architectures (LFADS top, STNDT bottom) were trained on neural recordings from monkeys performing a maze task, the `mc_maze_20` benchmark (Churchland et al., 2010; Pei et al., 2021). Distance to ground truth was approximated by the cross-decoding column average $\langle \mathcal{D}_{u \rightarrow v} \rangle_u$ (Fig. 19). Few-shot ($k = 128$) co-smoothing scores (left) negatively correlate with μ , while regular co-smoothing (right) does not. Green and red arrows indicate the extreme models whose latents are visualised in Fig. 19 matched by box/arrow colours. Q_v values may be compared against an EvalAI leaderboard (Pei et al., 2021). Note that we evaluate using an offline train-test split, not the true test set used for the leaderboard scores, for which held-out neuron data is not directly accessible.

While the combination of student-teacher and SOTA results put forth a compelling argument, we address here a few limitations of our work. Firstly, our SOTA results use only one of the datasets in the benchmark suite (Pei et al., 2021). With regard to the few-shot regression, while the bernoulli HMM scenario has a closed form solution: the maximum likelihood estimate, the poisson GLM regression for the SOTA models is optimised iteratively and is sensitive to the l2 hyperparameter `alpha`. In our results we select k and α that distinguish models in our candidate model sets giving moderate/high few-shot scores for some models and low scores to others. This is an empirical choice that must be made for each dataset and model-set. The few-shot training of g' is computationally inexpensive and may be thus can be evaluated over a range of values to find the ideal ones.

Overall, our work advances latent dynamics inference in general and prediction frameworks in particular. By exposing a failure mode of standard prediction metrics, we can guide the design of inference algorithms that take this into account. Furthermore, the few-shot prediction can be

incorporated into existing benchmarks and help guide the community to build models that are closer to the desired goal of uncovering latent dynamics in the brain.

References

- Bansal, Y., Nakkiran, P., and Barak, B. Revisiting model stitching to compare neural representations. In Ranzato, M., Beygelzimer, A., Dauphin, Y., Liang, P., and Vaughan, J. W. (eds.), *Advances in Neural Information Processing Systems*, volume 34, pp. 225–236. Curran Associates, Inc., 2021. URL https://proceedings.neurips.cc/paper_files/paper/2021/file/01ded4259d101feb739b06c399e9cd9c-Paper.pdf.
- Barak, O. Recurrent neural networks as versatile tools of neuroscience research. *Current opinion in neurobiology*, 46:1–6, 2017.
- Barber, D. *Bayesian reasoning and machine learning*. Cambridge University Press, 2012.
- Bauwens, L. and Veredas, D. The stochastic conditional duration model: a latent variable model for the analysis of financial durations. *Journal of econometrics*, 119(2): 381–412, 2004.
- Brenner, M., Koppe, G., and Durstewitz, D. Multimodal teacher forcing for reconstructing nonlinear dynamical systems. *arXiv preprint arXiv:2212.07892*, 2022.
- Churchland, M. M., Cunningham, J. P., Kaufman, M. T., Ryu, S. I., and Shenoy, K. V. Cortical preparatory activity: representation of movement or first cog in a dynamical machine? *Neuron*, 68(3):387–400, 2010.
- Deng, J., Dong, W., Socher, R., Li, L.-J., Li, K., and Fei-Fei, L. Imagenet: A large-scale hierarchical image database. In *2009 IEEE Conference on Computer Vision and Pattern Recognition*, pp. 248–255, 2009. doi: 10.1109/CVPR.2009.5206848.
- Durstewitz, D., Koppe, G., and Thurm, M. I. Reconstructing computational system dynamics from neural data with recurrent neural networks. *Nature Reviews Neuroscience*, 24(11):693–710, 2023.
- Gokcen, E., Jasper, A. I., Semedo, J. D., Zandvakili, A., Kohn, A., Machens, C. K., and Yu, B. M. Disentangling the flow of signals between populations of neurons. *Nature Computational Science*, 2(8):512–525, 2022.
- Hastie, T., Montanari, A., Rosset, S., and Tibshirani, R. J. Surprises in high-dimensional ridgeless least squares interpolation. *Annals of statistics*, 50(2):949, 2022.

- Huang, X. S., Perez, F., Ba, J., and Volkovs, M. Improving transformer optimization through better initialization. In *International Conference on Machine Learning*, pp. 4475–4483. PMLR, 2020.
- Keeley, S., Aoi, M., Yu, Y., Smith, S., and Pillow, J. W. Identifying signal and noise structure in neural population activity with gaussian process factor models. In Larochelle, H., Ranzato, M., Hadsell, R., Balcan, M., and Lin, H. (eds.), *Advances in Neural Information Processing Systems*, volume 33, pp. 13795–13805. Curran Associates, Inc., 2020. URL https://proceedings.neurips.cc/paper_files/paper/2020/file/9eed867b73ab1eab60583c9d4a789b1b-Paper.pdf.
- Keshtkaran, M. R., Sedler, A. R., Chowdhury, R. H., Tandon, R., Basrai, D., Nguyen, S. L., Sohn, H., Jazayeri, M., Miller, L. E., and Pandarinath, C. A large-scale neural network training framework for generalized estimation of single-trial population dynamics. *Nature Methods*, 19(12):1572–1577, 2022.
- Kingma, D. P. Auto-encoding variational bayes. *arXiv preprint arXiv:1312.6114*, 2013.
- Kingma, D. P. and Ba, J. Adam: A method for stochastic optimization. *arXiv preprint arXiv:1412.6980*, 2014.
- Koppe, G., Toutounji, H., Kirsch, P., Lis, S., and Durstewitz, D. Identifying nonlinear dynamical systems via generative recurrent neural networks with applications to fmri. *PLoS computational biology*, 15(8):e1007263, 2019.
- Le, T. and Shlizerman, E. Stndt: Modeling neural population activity with spatiotemporal transformers. In Koyejo, S., Mohamed, S., Agarwal, A., Belgrave, D., Cho, K., and Oh, A. (eds.), *Advances in Neural Information Processing Systems*, volume 35, pp. 17926–17939. Curran Associates, Inc., 2022. URL https://proceedings.neurips.cc/paper_files/paper/2022/file/72163d1c3c1726f1c29157d06e9e93c1-Paper-Conference.pdf.
- Lenc, K. and Vedaldi, A. Understanding image representations by measuring their equivariance and equivalence. In *2015 IEEE Conference on Computer Vision and Pattern Recognition (CVPR)*, pp. 991–999, 2015. doi: 10.1109/CVPR.2015.7298701.
- Macke, J. H., Buesing, L., Cunningham, J. P., Yu, B. M., Shenoy, K. V., and Sahani, M. Empirical models of spiking in neural populations. In Shawe-Taylor, J., Zemel, R., Bartlett, P., Pereira, F., and Weinberger, K. (eds.), *Advances in Neural Information Processing Systems*, volume 24. Curran Associates, Inc., 2011. URL https://proceedings.neurips.cc/paper_files/paper/2011/file/7143d7fbadfa4693b9eec507d9d37443-Paper.pdf.
- Maheswaranathan, N., Williams, A., Golub, M., Ganguli, S., and Sussillo, D. Universality and individuality in neural dynamics across large populations of recurrent networks. *Advances in neural information processing systems*, 32, 2019.
- Meghanath, G., Jimenez, B., and Makin, J. G. Inferring population dynamics in macaque cortex. *Journal of Neural Engineering*, 20(5):056041, nov 2023. doi: 10.1088/1741-2552/ad0651. URL <https://dx.doi.org/10.1088/1741-2552/ad0651>.
- Morcos, A., Raghu, M., and Bengio, S. Insights on representational similarity in neural networks with canonical correlation. In Bengio, S., Wallach, H., Larochelle, H., Grauman, K., Cesa-Bianchi, N., and Garnett, R. (eds.), *Advances in Neural Information Processing Systems*, volume 31. Curran Associates, Inc., 2018. URL https://proceedings.neurips.cc/paper_files/paper/2018/file/a7a3d70c6d17a73140918996d03c014f-Paper.pdf.
- Mullen, T. S., Schimel, M., Hennequin, G., Machens, C. K., Orger, M., and Jouary, A. Learning interpretable control inputs and dynamics underlying animal locomotion. In *The Twelfth International Conference on Learning Representations*, 2024. URL <https://openreview.net/forum?id=MFCjgEOLJT>.
- Nguyen, T. Q. and Salazar, J. Transformers without tears: Improving the normalization of self-attention. In *Proceedings of the 16th International Conference on Spoken Language Translation*, 2019.
- Pals, M., Sağtekin, A. E., Pei, F., Gloeckler, M., and Macke, J. H. Inferring stochastic low-rank recurrent neural networks from neural data. *arXiv preprint arXiv:2406.16749*, 2024.
- Pandarinath, C., O’Shea, D. J., Collins, J., Jozefowicz, R., Stavisky, S. D., Kao, J. C., Trautmann, E. M., Kaufman, M. T., Ryu, S. I., Hochberg, L. R., et al. Inferring single-trial neural population dynamics using sequential autoencoders. *Nature methods*, 15(10):805–815, 2018.
- Pei, F., Ye, J., Zoltowski, D., Wu, A., Chowdhury, R., Sohn, H., O’Doherty, J., Shenoy, K. V., Kaufman, M., Churchland, M., Jazayeri, M., Miller, L., Pillow, J., Park, I. M., Dyer, E., and Pandarinath, C. Neural

- latents benchmark '21: Evaluating latent variable models of neural population activity. In Vanschoren, J. and Yeung, S. (eds.), *Proceedings of the Neural Information Processing Systems Track on Datasets and Benchmarks*, volume 1. Curran, 2021. URL https://datasets-benchmarks-proceedings.neurips.cc/paper_files/paper/2021/file/979d472a84804b9f647bc185a877a8b5-Paper-round2.pdf.
- Perkins, S. M., Cunningham, J. P., Wang, Q., and Churchland, M. M. Simple decoding of behavior from a complicated neural manifold. *BioRxiv*, pp. 2023–04, 2023.
- Schimel, M., Kao, T.-C., Jensen, K. T., and Hennequin, G. iLQR-VAE : control-based learning of input-driven dynamics with applications to neural data. In *International Conference on Learning Representations*, 2022. URL <https://openreview.net/forum?id=wRODLdHaAiW>.
- Sedler, A. R. and Pandarinath, C. Ifads-torch: A modular and extensible implementation of latent factor analysis via dynamical systems. *arXiv preprint arXiv:2309.01230*, 2023.
- Sedler, A. R., Versteeg, C., and Pandarinath, C. Expressive architectures enhance interpretability of dynamics-based neural population models. *arXiv preprint arXiv:2212.03771*, 2022.
- She, Q. and Wu, A. Neural dynamics discovery via gaussian process recurrent neural networks. In Adams, R. P. and Gogate, V. (eds.), *Proceedings of The 35th Uncertainty in Artificial Intelligence Conference*, volume 115 of *Proceedings of Machine Learning Research*, pp. 454–464. PMLR, 22–25 Jul 2020. URL <https://proceedings.mlr.press/v115/she20a.html>.
- Shmueli, G. To Explain or to Predict? *Statistical Science*, 25(3):289–310, August 2010. ISSN 0883-4237, 2168-8745. doi: 10.1214/10-STS330. URL <https://projecteuclid.org/journals/statistical-science/volume-25/issue-3/To-Explain-or-to-Predict/10.1214/10-STS330.full>. Publisher: Institute of Mathematical Statistics.
- Sorscher, B., Ganguli, S., and Sompolinsky, H. Neural representational geometry underlies few-shot concept learning. *Proceedings of the National Academy of Sciences*, 119(43):e2200800119, 2022. doi: 10.1073/pnas.2200800119. URL <https://www.pnas.org/doi/abs/10.1073/pnas.2200800119>.
- Sussillo, D. and Barak, O. Opening the black box: low-dimensional dynamics in high-dimensional recurrent neural networks. *Neural computation*, 25(3):626–649, 2013.
- Valente, A., Pillow, J. W., and Ostojic, S. Extracting computational mechanisms from neural data using low-rank RNNs. In Oh, A. H., Agarwal, A., Belgrave, D., and Cho, K. (eds.), *Advances in Neural Information Processing Systems*, 2022. URL <https://openreview.net/forum?id=M12autRxeeS>.
- Versteeg, C., Sedler, A. R., McCart, J. D., and Pandarinath, C. Expressive dynamics models with nonlinear injective readouts enable reliable recovery of latent features from neural activity. *arXiv preprint arXiv:2309.06402*, 2023.
- Vinuesa, R. and Brunton, S. L. Enhancing computational fluid dynamics with machine learning. *Nature Computational Science*, 2(6):358–366, 2022.
- Vyas, S., Golub, M. D., Sussillo, D., and Shenoy, K. V. Computation through neural population dynamics. *Annual review of neuroscience*, 43:249–275, 2020.
- Wu, A., Roy, N. A., Keeley, S., and Pillow, J. W. Gaussian process based nonlinear latent structure discovery in multivariate spike train data. In Guyon, I., Luxburg, U. V., Bengio, S., Wallach, H., Fergus, R., Vishwanathan, S., and Garnett, R. (eds.), *Advances in Neural Information Processing Systems*, volume 30. Curran Associates, Inc., 2017. URL https://proceedings.neurips.cc/paper_files/paper/2017/file/b3b4d2dbedc99fe843fd3dedb02f086f-Paper.pdf.
- Wu, A., Pashkovski, S., Datta, S. R., and Pillow, J. W. Learning a latent manifold of odor representations from neural responses in piriform cortex. In Bengio, S., Wallach, H., Larochelle, H., Grauman, K., Cesa-Bianchi, N., and Garnett, R. (eds.), *Advances in Neural Information Processing Systems*, volume 31. Curran Associates, Inc., 2018. URL https://proceedings.neurips.cc/paper_files/paper/2018/file/17b3c7061788dbe82de5abe9f6fe22b3-Paper.pdf.
- Ye, J. and Pandarinath, C. Representation learning for neural population activity with neural data transformers. *arXiv preprint arXiv:2108.01210*, 2021.
- Yu, B. M., Cunningham, J. P., Santhanam, G., Ryu, S., Shenoy, K. V., and Sahani, M. Gaussian-process factor analysis for low-dimensional single-trial analysis of neural population activity. In Koller, D., Schuurmans, D., Bengio, Y., and Bottou, L. (eds.), *Advances in Neural Information Processing Systems*, volume 21. Curran Associates, Inc.,

2008. URL https://proceedings.neurips.cc/paper_files/paper/2008/file/ad972f10e0800b49d76fed33a21f6698-Paper.pdf.

Zhao, Y. and Park, I. M. Variational Latent Gaussian Process for Recovering Single-Trial Dynamics from Population Spike Trains. *Neural Computation*, 29(5):1293–1316, 05 2017. ISSN 0899-7667. doi: 10.1162/NECO_a_00953. URL https://doi.org/10.1162/NECO_a_00953.

A. Additional discussion

Why use HMMs? The SOTA LVMs are typically deep-neural networks. HMMs are much too simple.

Real neural data is *trajectories across time*, and therefore a teacher model should be a dynamical system. HMMs were chosen as a tractable dynamical system to show our claims. We highlight specific properties of HMMs that are relevant to our use:

- HMMs are perhaps the simplest stochastic dynamical system, making analysis and visualisation possible, e.g., the graphs shown in Fig. 2 show that the students contain the teacher’s dynamics – a valuable insight,
- HMMs are expressive enough to capture real neural dynamics. Indeed, HMMs appear on the leaderboard for the `mc_maze_20` benchmark (see [here](#)). Although not the leading models, they outperform other baselines.
- They may be used for both data generation and inference of latents – perhaps the simplest Latent Variable Models for time-series data. By constraining the student and teacher to the same class of models, we are justified in directly comparing the two.

How to choose k ?

As k is increased, the ability of the few-shot metric to discriminate extraneous dynamics decreases. The exact manner depends on the setting (see theoretical analysis in appendices L, M, N). On the other hand, decreasing k too much increases noise, and eventually precludes reaching any conclusion. Appendix H provides practical advice on the choice of k in real-world scenarios.

Why use cross-decoding as a proxy, and not directly to evaluate models instead of few-shot co-smoothing?

In the HMM setting, we see that indeed cross-decoding is more correlated to ground truth than few-shot co-smoothing (figures 4 and 10). Nevertheless, it is qualitatively different from few-shot co-smoothing and has several disadvantages. First, the computational cost is high because it requires training a population of models and comparing between all directed pairs of them. Furthermore, it is also less universal and standardised than few-shot co-smoothing, as it is dependent on a specific ‘jury’ of models – the population itself. On the other hand, few-shot co-smoothing is computed for each model independently. Furthermore, its close relation to co-smoothing, the current standard for benchmarking neural LVMs, makes it easier to incorporate into existing benchmarking pipelines. For these reasons, we identify few-shot co-smoothing as the better option for evaluation.

Scope of applicability. How general are the conclusions from the HMM student-teacher experiments? There is a large gap between HMMs and modern SOTA models discussed in the main text.

Both our theoretical and experimental results extend beyond HMMs. Theoretically, we show that few-shot regression is sensitive to extraneous dynamics in three different settings (appendices L, M, N). In all three settings, the true and extraneous latent representations are distinguished by poorer generalisation performance of the few-shot regression for the extraneous model at some finite k and the difference vanishes as $k \rightarrow \infty$. Experimentally, we replicate the HMM results in a continuous setting – Linear Gaussian State Space Models (LGSSMs) in appendix E. The SOTA results in the main text are an additional experimental validation.

If you want simple students, why not use regularization on the latents?

Previous work also noted that students can predict well despite having the wrong latents (Sedler et al., 2022). To alleviate this, regularization on the latents was suggested (Sedler et al., 2022; Versteeg et al., 2023). Our approach is different in that we remain within the **latent-agnostic** prediction framework. Despite not requiring access to the latents, few-shot prediction encourages models without extraneous dynamics. This implicit form of regularization has the advantage of being easily integrated within benchmarks and allowing optimization of algorithms without restriction.

Does few-shot co-smoothing replace regular co-smoothing?

No. We propose few-shot co-smoothing as a secondary metric to accompany regular co-smoothing. The latter encourages the student to contain as much of the teacher dynamics as possible, while the former encourages the student to have as little extraneous dynamics differing from that of the teacher. We show that student models with good performance in both metrics, are the students most similar to the teacher.

B. Hidden Markov Model training

HMMs are traditionally trained with expectation maximisation, but they can also be trained using gradient-based methods. We focus here on the latter as these are used ubiquitously and apply to a wide range of architectures. We use an existing implementation of HMMs with differentiable parameters: `dynamax` – a library of differentiable state-space models built with `jax`.

We seek HMM parameters $\theta := (A, B^{[\text{in}, \text{out}]}, \pi)$ that minimise the negative log-likelihood loss, L of the held-in and held-out neurons in the train trials:

$$L(\theta; \mathcal{X}_{[\text{in}, \text{out}]}^{\text{train}}) = -\log p(\mathcal{X}_{[\text{in}, \text{out}]}^{\text{train}}; \theta) \quad (14)$$

$$= \sum_{i \in \text{train}} -\log p\left(\left(X_{1:T, [\text{in}, \text{out}]}\right)^{(i)}; \theta\right) \quad (15)$$

To find the minimum we do full-batch gradient descent on L , using `dynamax` together with the Adam optimiser (Kingma & Ba, 2014).

C. Decoding across HMM latents: fitting and evaluation

Consider two HMMs u and v , of sizes $M(u)$ and $M(v)$, both candidate models of a dataset \mathcal{X} . Following equation 7, each HMM can be used to infer latents from the data, defining encoder mappings f^u and f^v . These map a single trial i of the data $(\mathbf{X}_{:, \text{in}})^{(i)} \in \mathcal{X}$ to $(\boldsymbol{\xi}_t^{(i)})_u$ and $(\boldsymbol{\xi}_t^{(i)})_v$.

We now perform a multinomial regression from $(\boldsymbol{\xi}_t^{(i)})_u$ to $(\boldsymbol{\xi}_t^{(i)})_v$.

$$\mathbf{p}_t^{(i)} = h\left(\left(\boldsymbol{\xi}_t^{(i)}\right)_u\right) \quad (16)$$

$$h(\boldsymbol{\xi}) = \sigma(W\boldsymbol{\xi} + \mathbf{b}) \quad (17)$$

where $W \in \mathbb{R}^{M(v) \times M(u)}$, $\mathbf{b} \in \mathbb{R}^{M(v)}$ and σ is the softmax. During training we sample states from the target PMFs $(z_t^{(i)})_v \sim (\boldsymbol{\xi}_t^{(i)})_v$ thus arriving at a more well know problem scenario: classification of $M(v)$ -classes. We optimize W and \mathbf{b} to minimise a cross-entropy loss to the target $(z_t^{(i)})_v$ using the `fit()` method of `sklearn.linear_model.LogisticRegression`.

We define decoding error, as the average Kullback-Leibler divergence D_{KL} between target and predicted distributions:

$$\mathcal{D}_{u \rightarrow v} := \frac{1}{S^{\text{test}} T} \sum_{i \in \text{test}} \sum_{t=1}^T D_{KL}\left(\mathbf{p}_t^{(i)}, (\boldsymbol{\xi}_t^{(i)})_v\right) \quad (18)$$

where D_{KL} is implemented with `scipy.special.relentr`.

In section 4 and Fig. 1, the data X is sampled from a single teacher HMM, T, and we evaluate $\mathcal{D}_{T \rightarrow S}$ and $\mathcal{D}_{S \rightarrow T}$ for each student notated simply as S.

D. Few-shot co-smoothing is not simply hard co-smoothing

The few-shot benchmark is a more difficult one than standard co-smoothing. Thus, it might seem that any increase in the difficulty of the benchmark will yield similar results. To show this is not the case, we use standard co-smoothing with fewer held-in neurons (Fig. 7). The score is lower (because it's more difficult), but does not discriminate models.

E. Student-teacher results in Linear Gaussian State Space Models

We demonstrate that our results are not unique to the HMM setting by simulating another simple scenario: linear gaussian state space models (LGSSM), i.e., Kalman Smoothing.

The model is defined by parameters $(\boldsymbol{\mu}_0, \boldsymbol{\Sigma}_0, \mathbf{F}, \mathbf{G}, \mathbf{H}, \mathbf{R})$. A major difference to HMMs is that the latent states $\mathbf{z} \in \mathbb{R}^M$ are continuous. They follow the dynamics given by:

$$\mathbf{z}_0 \sim \mathcal{N}(\boldsymbol{\mu}_0, \boldsymbol{\Sigma}_0) \quad (19)$$

$$\mathbf{z}_t \sim \mathcal{N}(\mathbf{F}\mathbf{z}_{t-1} + \mathbf{b}, \mathbf{G}) \quad (20)$$

$$\mathbf{x}_t \sim \mathcal{N}(\mathbf{H}\mathbf{z}_t + \mathbf{c}, \mathbf{R}) \quad (21)$$

Given these dynamics, the latents \mathbf{z} can be inferred from observations \mathbf{x} using Kalman smoothing, analogous to equation 7. Here we use the jax based `dynamax` implementation.

As with HMMs we use a teacher LGSSM with $M = 4$, with parameters chosen randomly (using the `dynamax` defaults) and then fixed. Student LGSSMs are also initialised randomly and optimised with Adam (Kingma & Ba, 2014) to minimise negative loglikelihood on the training data (see table 1 for dimensions of the synthetic data set). $\mathcal{D}_{S \rightarrow T}$ and $\mathcal{D}_{T \rightarrow S}$ is computed with linear regression (`sklearn.linear_model.LinearRegression`) and predictions are evaluated against the target using R^2 (`sklearn.metrics.r2_score`). We define $\mathcal{D}_{u \rightarrow v} := 1 - (R^2)_{u \rightarrow v}$. Few-shot regression from \mathbf{z} to $\mathbf{x}^{k\text{-out}}$ is also performed using linear regression.

In line with our results with HMMs (sections 4 and 5), in Fig. 8 we show that among the models with high test loglikelihood (> -55), $\mathcal{D}_{S \rightarrow T}$, but not $\mathcal{D}_{T \rightarrow S}$, is highly correlated to test loglikelihood, while $\mathcal{D}_{T \rightarrow S}$ shows a close relationship to Average 10 shot MSE error.

F. Analysis of SOTA models

We denote the set of high co-smoothing models as those satisfying $\mathcal{Q}_{\text{model}} > \mathcal{Q}_{\text{best model}} - \epsilon$, choosing $\epsilon = 5 \times 10^{-3}$ for LFADS and $\epsilon = 1.3 \times 10^{-2}$ for STNDT. $\mathcal{F} := \{(f_u, g_u)\}_{u=1}^U$, the encoders and decoders respectively. Note that both architectures are deep neural networks given by the composition $g \circ f$, and the choice of intermediate layer whose activity is deemed the ‘latent’ \mathbf{Z} is arbitrary. Here we consider g the last ‘read-out’ layer and f to represent all the layers up-to g . g takes the form of Poisson Generalised Linear Model (GLM), a natural and simple choice for the few-shot version g' . To this end, we use `sklearn.linear_model.PoissonRegressor`. The poisson regressor has a hyperparameter alpha, the amount of l2 regularisation. For the results in the main text, $\langle \mathcal{Q}_v^k \rangle$ in Fig. 6, we select $\alpha = 10^{-3}$.

To perform few-shot co-smoothing, we partition the train data into several subsets of k trials. To implement this in a standardised way, we build upon the `nlb_tools` library (appendix J). This way we ensure that all models are trained and tested on identical partitions.

We perform a cross-decoding from the latents of model u , $(\mathbf{Z}_{t,:})_u$, to those of model v , $(\mathbf{Z}_{t,:})_v$, for every pair of models u and v using a linear mapping $h(\mathbf{z}) := \mathbf{W}\mathbf{z} + \mathbf{b}$ implemented with `sklearn.linear_model.LinearRegression`:

$$\left(\hat{\mathbf{Z}}_{t,:}^{(i)} \right)_v = h_{u \rightarrow v} \left(\left(\mathbf{Z}_{t,:}^{(i)} \right)_u \right) \quad (22)$$

minimising a mean squared error loss. We then evaluate a R^2 score (`sklearn.metrics.r2_score`) of the predictions, $(\hat{\mathbf{Z}})_v$, and the target, $(\mathbf{Z})_v$, for each mapping. We define the decoding error $\mathcal{D}_{u \rightarrow v} := 1 - (R^2)_{u \rightarrow v}$. The results are accumulated into a $U \times U$ matrix (see Fig. 19).

G. Validating cross-decoding column-mean as a proxy of ground truth distance in HMMs

For SOTA models, we don’t have ground truth and therefore use cross-decoding as a proxy. We validate this approach in the HMM setting, where we can compute cross-decoding among student models, while also having access to ground truth, i.e., the teacher. As Fig. 9 shows, the novel cross-decoding metric is highly correlated to the ground truth metric of interest $\mathcal{D}_{T \rightarrow S}$.

Next, in Fig. 10 we replicate the comparison in Fig. 6 of the main text, with the HMMs instead of SOTA models. Despite very different LVM architectures and very different datasets (synthetic versus real neural data), the results are strikingly similar.

Table 1. Dimensions of real and synthetic datasets. Number of train and test trials S^{train} , S^{test} , time-bins per trial for co-smoothing T , and forward-prediction T^{fp} , held-in, held-out and k -out neurons N^{in} , N^{out} , $N^{k\text{-out}}$.

DATASET	S^{TRAIN}	S^{TEST}	T	T^{FP}	N^{IN}	N^{OUT}	$N^{k\text{-OUT}}$
SYNTHETIC HMM	2000	100	10	–	20	50	50
SYNTHETIC LGSSM (APPENDIX E)	20	500	10	–	5	30	30
NLB <small>mc_maze_20</small> (PEI ET AL., 2021; CHURCHLAND ET AL., 2010)	1721	574	35	10	127	55	55 ²

Taken together, these results reinforce our use of the novel cross-decoding metric as a proxy to $\mathcal{D}_{T \rightarrow S}$ for SOTA models on real data where there is no access to ground truth, i.e., no teacher model T.

H. How to choose k and s ?

We define Q^k the k -shot co-smoothing score: the co-smoothing score given by predictions from decoder g' trained with only k trials of the k -out neurons and the corresponding latents given by the encoder f (section 5 and Fig. 3). As this can be variable across random k -trial subsets we report the average k -shot co-smoothing, $\langle Q^k \rangle$, averaging over s decoders each independently trained on random resamples of k -trials. Here we report how the results change with k , offering guidelines on how to choose k and s .

We first analyse the student-teacher HMMs from 4. In Fig. 11 we show several quantities as a function of k . We see that small k maximally separates two extreme models and the scores converge for $k \rightarrow \infty$. However at small k , scores Q^k from single models are also more variable, therefore more resamples s are required for a good estimate of the mean $\langle Q^k \rangle$. We choose $s := \lfloor \frac{S_{\text{train}}}{k} \rfloor$ and find that $k \approx 6$ gives us the best correlation to ground-truth measure (Fig. 11 bottom-right).

We do a similar analysis for LFADS models on the mc_maze_20 dataset. In Fig. 12 we show several values of Q^k (appendix F) for several random samples of k -trials, and at various values of k . We find that for k values including and below $k = 32$, scores are negative, and at $k = 4$ scores are even worse and vary by orders of magnitude. Among the values we checked, we found $k = 128$ to be the smallest value with positive and low-variance Q^k . Thus, in Fig. 6 we use an intermediate value of $k = 128$ and $s := \lfloor \frac{S_{\text{train}}}{k} \rfloor$.

I. Dimensions of datasets

We analyse three datasets in this work. Two synthetic datasets generated by an HMM (ground truth in Fig. 2), an LGSSM (appendix E) and the mc_maze_20 dataset from the Neural Latent Benchmarks (NLB) suite (Pei et al., 2021; Churchland et al., 2010). In table 1, we summarise the dimensions of these datasets. To evaluate k -shot on the existing SOTA methods while maintaining the NLB evaluations, we conserved the *forward-prediction* aspect. During model training, models output rate predictions for T^{fp} future time bins in each trial, i.e., equation 1 and equation 2 are evaluated for $1 \leq t \leq T^{\text{fp}}$ while input remains as $X_{1:T,\text{in}}$. Although we do not discuss the forward-prediction metric in our work, we note that the SOTA models receive gradients from this portion of the data.

In mc_maze_20 we reuse held-out neurons as k -out neurons. We do this to preserve NLB evaluation metrics on the SOTA models, as opposed to re-partitioning the dataset resulting in different scores from previous works. This way existing co-smoothing scores are preserved and k -shot co-smoothing scores can be directly compared to the original co-smoothing scores. The downside is that we are not testing the few-shot on ‘novel’ neurons. Our numerical results (Fig. 6) show that our concept still applies.

J. Code repositories

The experiments done in this work are largely based on code repositories from previous works. The code developed here is in https://osf.io/4bckn/?view_only=73b3aee9a8eb43e8bb3b286c800c6448. Table 2 provides links to the code repositories used or developed in this work.

²In mc_maze_20 we use the same set of neurons for N^{out} and $N^{k\text{-out}}$.

Table 2. Summary of key repositories used in this paper

REPOSITORY	FORKED FROM	CITATIONS
ANONYMOUS REPO	HTTPS://GITHUB.COM/NEURALLATENTS/NLB_TOOLS	(PEI ET AL., 2021)
ANONYMOUS REPO	HTTPS://GITHUB.COM/TRUNGLE93/STNDT	(LE & SHLIZERMAN, 2022; YE & PANDARINATH, 2021; PEI ET AL., 2021; NGUYEN & SALAZAR, 2019; HUANG ET AL., 2020)
ANONYMOUS REPO	HTTPS://GITHUB.COM/ARSEDLER9/LFADS-TORCH	(SEDLER & PANDARINATH, 2023; PANDARINATH ET AL., 2018; KESHTKARAN ET AL., 2022)

K. Compatibility and consistency of cross-decoding across LVM architectures

In this section we analyse the cross-decoding approach, pooling together the SOTA models from the two architectures: STNDT and LFADS, all trained on the same `mc_maze_20` dataset. We filtered models to those with near-SOTA co-smoothing, specifically $0.348 < Q < 0.36$, resulting in 75 LFADS and 40 STNDT models. Note that this included LFADS models which were not in the main text Fig. 6.

Fig. 13 shows the cross-decoding matrix $\mathcal{D}_{u \rightarrow v}$ for all pairs of models (u, v) in this combined set, as computed in section 7 and appendix F. The cross-decoding matrix reveals a block structure, suggesting larger decoding errors for model pairs from different architectures versus model pairs within the same architecture. Crucially, on top of this block structure, we see clear continuation of columns. This implies that models that are extraneous in one class are also judged as extraneous by the other class. This is summarised in Fig. 14, where we compare column means for each model over the ‘same architecture pool’ and ‘other architecture pool’. Thus, cross decoding can be used across architectures. One should note, however, that having an unbalanced sample from the two classes could bias scores to be lower for the larger class. Finally, we use the combined cross-decoding matrix to repeat the analysis of the main text, but combining both model types. Fig. 15 shows that our conclusions hold – co-smoothing is uncorrelated with cross-decoding, while few-shot is correlated.

L. Theoretical analysis of ridgeless least squares regression with extraneous noise

Teacher latents $z_i^* \sim \mathcal{N}(0, 1)$ generate observations x_i :

$$x_i = z_i^* + \epsilon_i, \tag{23}$$

where $\epsilon_i \sim \mathcal{N}(0, \sigma_{\text{obs}}^2)$ is observation noise.

In this setup there is no time index: we consider only a single sample index i .

We consider candidate student latents, $\mathbf{z} \in \mathbb{R}^p$, that *contain* the teacher along with extraneous noise, i.e:

$$\mathbf{z}_i := [z_i^* \quad \boldsymbol{\xi}_i]^T, \tag{24}$$

where $\boldsymbol{\xi}_i \sim \mathcal{N}(0, \sigma_{\text{ext}}^2 \mathbf{I}_{p-1})$ is a vector of i.i.d. extraneous noise, and \mathbf{I}_{p-1} is the $(p-1) \times (p-1)$ identity matrix.

We study the minimum l_2 norm least squares regression estimator on k training samples:

$$\hat{\mathbf{w}} = \arg \min \left\{ \|\mathbf{w}\|_2 : \mathbf{w} \text{ minimizes } \sum_{i=1}^k \|x_i - \mathbf{w}^T \mathbf{z}_i\|_2^2 \right\}. \tag{25}$$

with the regression weights $\mathbf{w} \in \mathbb{R}^p$. More succinctly, $\mathbf{z}_i \sim \mathcal{N}(0, \Sigma)$, where $\Sigma = \text{diag}([1, \sigma_{\text{ext}}^2, \dots, \sigma_{\text{ext}}^2])$.

Note that, by construction, the true mapping is:

$$\mathbf{w}^* = [1 \quad 0 \quad \dots \quad 0]^T. \quad (26)$$

Test loss or *risk* is a mean squared error:

$$R(\hat{\mathbf{w}}; \mathbf{w}^*) = \mathbb{E}_{\mathbf{z}_0} (\mathbf{z}_0^T \mathbf{w}^* - \mathbf{z}_0^T \hat{\mathbf{w}})^2, \quad (27)$$

given a test sample \mathbf{z}_0 . The error can be decomposed as:

$$R(\hat{\mathbf{w}}; \mathbf{w}^*) = \underbrace{\|\mathbb{E}(\hat{\mathbf{w}}) - \mathbf{w}^*\|_{\Sigma}^2}_{\text{bias, } B} + \underbrace{\text{Tr}[\text{Cov}(\hat{\mathbf{w}})\Sigma]}_{\text{variance, } V}, \quad (28)$$

The scenario described above is a special case of (Hastie et al., 2022). What follows is a direct application of their theory, which studies the risk R , in the limit $k, p \rightarrow \infty$ such that $p/k \rightarrow \gamma \in (0, \infty)$, to our setting. The alignment of the theory with numerical simulations is demonstrated in Fig. 16.

Claim 1. $\gamma < 1$, i.e., the underparameterised case $k > p$.

$B = 0$ and the risk is just variance and is given by:

$$\lim_{k, p \rightarrow \infty \text{ and } p/k \rightarrow \gamma} R(\hat{\mathbf{w}}; \mathbf{w}^*) = \sigma_{\text{obs}}^2 \frac{\gamma}{1 - \gamma}, \quad (29)$$

with no dependence on σ_{ext} .

Proof. This is a direct restatement of Proposition 2 in (Hastie et al., 2022). □

Claim 2. $\gamma > 1$, i.e., the overparameterised case $k < p$.

The following is true as $k, p \rightarrow \infty$ and $p/k \rightarrow \gamma$:

$$\lim_{k, p \rightarrow \infty \text{ and } p/k \rightarrow \gamma} B = \frac{\gamma(\gamma - 1)}{\left(\gamma - 1 + \frac{1}{\sigma_{\text{ext}}^2}\right)^2} \quad (30)$$

$$\lim_{k, p \rightarrow \infty \text{ and } p/k \rightarrow \gamma} V = \sigma_{\text{obs}}^2 \frac{\gamma}{\gamma - 1} \quad (31)$$

Proof. For the non-isotropic case (Hastie et al., 2022) define the following distributions based on the eigendecomposition of Σ .

$$d\hat{H}(s) = \frac{1}{p}\delta(s - 1) + \frac{p-1}{p}\delta(s - \sigma_{\text{ext}}^2) \quad (32)$$

$$d\hat{G}(s) = \delta(s - 1) \quad (33)$$

In the limit $p \rightarrow \infty$ we take $d\hat{H}(s) \approx \delta(s - \sigma_{\text{ext}}^2)$. This greatly simplifies calculations and nevertheless provide a good fit for numerical results with finite k and p . We solve for $c_0(\gamma, \hat{H})$ using equation 12 in (Hastie et al., 2022).

$$\gamma c_0 = \frac{1}{(\gamma - 1)\sigma_{\text{ext}}^2} \quad (34)$$

We then compute the limiting values of B and V :

$$B = \|w^*\|^2(1 + \gamma c_0 \sigma_{\text{ext}}^2) \frac{1}{(1 + \gamma c_0)^2} \quad (35)$$

$$V = \sigma_{\text{obs}}^2 \gamma c_0 \sigma_{\text{ext}}^2. \quad (36)$$

Substituting γc_0 completes the proof. \square

Comments:

- The extraneous noise, σ_{ext} , only affects the risk of ridgeless regression for $k < p$,
- moreover, it only affects the bias term not the variance.
- Observation noise only affects the variance term, therefore the dependence of the risk on σ_{ext} would occur even if $\sigma_{\text{obs}} = 0$, i.e., in the absence of observation noise.

M. Theoretical analysis of prototype learning for binary classification with extraneous noise

Teacher latents are distributed as $p(z_i^*) = \frac{1}{2}\delta(z_i^* - \frac{1}{\sqrt{2}}) + \frac{1}{2}\delta(z_i^* + \frac{1}{\sqrt{2}})$, that is either $\frac{1}{\sqrt{2}}$ or $-\frac{1}{\sqrt{2}}$ with probability $\frac{1}{2}$, representing two classes a and b respectively.

We consider candidate student latents, $\mathbf{z} \in \mathbb{R}^{2M+1}$, that *contain* the teacher along with extraneous noise, i.e:

$$\mathbf{z}_i := \begin{cases} \begin{bmatrix} z_i^* & \boldsymbol{\xi}_i & \mathbf{0} \end{bmatrix}^T & \text{if } z_i^* = 1 \\ \begin{bmatrix} z_i^* & \mathbf{0} & \boldsymbol{\xi}_i \end{bmatrix}^T & \text{if } z_i^* = -1 \end{cases} \quad (37)$$

where $\boldsymbol{\xi}_i \sim \mathcal{N}(0, \sigma_{\text{ext}}^2 \mathbf{I}_M)$ is a M -vector of i.i.d. extraneous noise, and \mathbf{I}_M is the $M \times M$ identity matrix and $\mathbf{0} \in \mathbb{R}^M$.

We consider the prototype learner $\mathbf{w} = \bar{\mathbf{z}}_a - \bar{\mathbf{z}}_b$, $\mathbf{b} = \frac{1}{2}(\bar{\mathbf{z}}_a + \bar{\mathbf{z}}_b)$, where $\bar{\mathbf{z}}_a$ and $\bar{\mathbf{z}}_b$ are the sample means of k latents from class a and k latents from class b respectively. The classification rule is given by the sign of $\mathbf{w}^T \mathbf{x} - \mathbf{b}$: classifying the input \mathbf{x} as a if positive and b otherwise.

This setting is a special case of (Sorscher et al., 2022). They provide a theoretical prediction for average few-shot classification error rate for class a , ϵ_a , given by $\epsilon_a = H(\text{SNR})$ where $H(x) = \frac{1}{\sqrt{2\pi}} \int_x^\infty dt \exp(-t^2/2)$ is a monotonously decreasing function.

$$\text{SNR}_a = \frac{1}{2} \frac{\|\Delta \mathbf{x}_0\|^2 + (R_b^2 R_a^2 - 1)/k}{\sqrt{D_a^{-1}/k + \|\Delta \mathbf{x}_0^T U_b\|^2/k + \|\Delta \mathbf{x}_0^T U_a\|^2}}. \quad (38)$$

$\Delta \mathbf{z} = \mathbf{z}_a - \mathbf{z}_b$ the difference of the population centroids of the two classes.

In our case this reduces to:

$$\text{SNR} \approx \frac{\sqrt{Mk}}{\sigma_{\text{ext}}^2} \quad (39)$$

To obtain this we note radii of manifold a is $[0 \ \sigma_{\text{ext}} \ \dots \ \sigma_{\text{ext}} \ 0 \ \dots \ 0]$ with an average radius $R = R_a = R_b = \frac{M}{(2M+1)} \sigma_{\text{ext}}^2$ and participation ratio $D_a = (\sum_i (R_a^i)^2)^2 / \sum_i (R_a^i)^4 = M$.

We substitute $\|\Delta \mathbf{x}_0\|^2 = \frac{1}{R^2} = \frac{2M+1}{M\sigma_{\text{ext}}^2} \approx \frac{2}{\sigma_{\text{ext}}^2}$.

The bias term $(R_b^2 R_a^2 - 1)/k$ is zero since $R_a = R_b$.

The $\Delta \mathbf{x}_0^T U_a$ and $\Delta \mathbf{x}_0^T U_b$ terms are both zero.

The participation ratio $D_a = M$. Our construction is symmetric in that $SNR_a = SNR_b$.

Comments:

- Classification error monotonously decreases with number of samples k , $\epsilon \rightarrow 0$ as $k \rightarrow \infty$, for all finite values of σ_{ext} .
- Classification error monotonously increases with extraneous noise σ_{ext} , significantly deviating from zero when $\sigma_{\text{ext}}^2 \approx \sqrt{Mk}$.

N. Theoretical analysis of few shot learning in HMMs

Consider a student-teacher scenario as in section 4. We let $T = 2$ and use a stationary teacher $z_1^{(i)} = z_2^{(i)}$. Now consider two examples of inferred students. To ensure a fair comparison, we use two latent states for both students. In the *good* student, ξ , these two states statistically do not depend on time, and therefore it does not have extraneous dynamics. In contrast, the *bad* student, μ , uses one state for the first time step, and the other for the second time step. A particular example of such students is:

$$\xi_t = [0.5 \quad 0.5]^T \quad t \in \{1, 2\} \quad (40)$$

$$\mu_{t=1} = [1 \quad 0]^T \quad \mu_{t=2} = [0 \quad 1]^T \quad (41)$$

where each vector corresponds to the two states, and we only consider two time steps.

We can now evaluate the maximum likelihood estimator of the emission matrix from k trials for both students. In the case of bernoulli HMMs the maximum likelihood estimate of g' given a fixed f and k trials has a closed form:

$$\hat{B}_{m,n} = \frac{\sum_{i \in k\text{-shot trials}} \sum_{t=1}^T \mathbb{I}[X_{t,n}^{(i)} = 1] \xi_{t,m}^{(i)}}{\sum_{i' \in k\text{-shot trials}} \sum_{t'=1}^T \xi_{t',m}^{(i')}} \quad \forall 1 \leq m \leq M \text{ and } n \in k\text{-out neurons} \quad (42)$$

We consider a single neuron, and thus omit n , reducing the estimates to:

$$\begin{aligned} \hat{B}_1(\xi) &= \frac{0.5(C_1 + C_2)}{0.5kT} & \hat{B}_1(\mu) &= \frac{C_1}{k} \\ \hat{B}_2(\xi) &= \frac{0.5(C_1 + C_2)}{0.5kT} & \hat{B}_2(\mu) &= \frac{C_2}{k} \end{aligned} \quad (43)$$

where C_t is the number of times $x = 1$ at time t in k trials. We see that C_t is a sum of k i.i.d. Bernoulli random variables (RVs) with the teacher parameter B^* , for both $t = 1, 2$.

Thus, $\hat{B}_m(\xi)$ and $\hat{B}_m(\mu)$ are scaled binomial RVs with the following statistics:

$$\begin{aligned} \mathbb{E} \hat{B}_1(\xi) &= \mathbb{E} \hat{B}_2(\xi) = B^* & \mathbb{E} \hat{B}_1(\mu) &= \mathbb{E} \hat{B}_2(\mu) = B^* \\ \text{Cov} \left[\hat{\mathbf{B}}(\xi) \right] &= \frac{1}{2k} B^* (1 - B^*) \begin{bmatrix} 1 & 1 \\ 1 & 1 \end{bmatrix} & \text{Cov} \left[\hat{\mathbf{B}}(\mu) \right] &= \frac{1}{k} B^* (1 - B^*) \begin{bmatrix} 1 & 0 \\ 0 & 1 \end{bmatrix} \end{aligned} \quad (44)$$

The test loss is given by $L(\hat{B}) = \mathbb{E} \frac{1}{T} \sum_t \log p(X_t^{(i)}; \hat{B}) = \frac{1}{T} \sum_t B^* \log(R_t) + (1 - B^*) \log(1 - R_t)$. For ξ , $R_t = 0.5(\hat{B}_1 + \hat{B}_2)$ for both values of t , and for μ , $R_1 = \hat{B}_1$ and $R_2 = \hat{B}_2$. Ultimately,

$$L_\xi(\hat{\mathbf{B}}(\xi)) = \frac{1}{T} \sum_t B^* \log \left(0.5(\hat{B}_1 + \hat{B}_2) \right) + (1 - B^*) \log \left(1 - 0.5(\hat{B}_1 + \hat{B}_2) \right) \quad (45)$$

$$L_\mu(\hat{\mathbf{B}}(\mu)) = \frac{1}{T} \sum_t B^* \log \left(\hat{B}_t \right) + (1 - B^*) \log \left(1 - \hat{B}_t \right) \quad (46)$$

To see how these variations affect the test loglikelihood L of the few-shot regression on average, we do a Taylor expansion around B^* , recognising that the function is maximised at B^* , so $\frac{\partial L}{\partial B}\Big|_{B^*} = 0$.

$$\mathbb{E}_{\hat{B}_k} L(\hat{B}_k) = \mathbb{E}_{\hat{B}_k} \left[L(B_\infty) + \frac{1}{2} (\hat{B}_k - B^*)^T \frac{\partial^2 L}{\partial B^2} \Big|_{B^*} (\hat{B}_k - B^*) + \dots \right] \quad (47)$$

$$\approx L(B^*) + \mathbb{E}_{\hat{B}_k} \frac{1}{2} (\hat{B}_k - B^*)^T \frac{\partial^2 L}{\partial B^2} \Big|_{B^*} (\hat{B}_k - B^*) \quad (48)$$

$$= L(B^*) + \underbrace{\frac{1}{2} (\mathbb{E} \hat{B}_k - B^*)^T \frac{\partial^2 L}{\partial B^2} \Big|_{B^*} (\mathbb{E} \hat{B}_k - B^*)}_{\text{bias}} + \underbrace{\frac{1}{2} \text{Tr} \left[\text{Cov}(\hat{B}_k) \frac{\partial^2 L}{\partial B^2} \Big|_{B^*} \right]}_{\text{variance}} \quad (49)$$

We see that this second order truncation of the loglikelihood is decomposed into a bias and a variance term. We recognise that the bias term goes to zero because we know the estimator is unbiased (equation 44). To compute the variance term, we compute the Hessians which differ for the two models:

$$\frac{\partial^2 L_\xi}{\partial B^2} \Big|_{B^*} = -\frac{\eta}{4} \begin{bmatrix} 1 & 1 \\ 1 & 1 \end{bmatrix}, \quad \frac{\partial^2 L_\mu}{\partial B^2} \Big|_{B^*} = -\frac{\eta}{2} \begin{bmatrix} 1 & 0 \\ 0 & 1 \end{bmatrix}, \quad (50)$$

where $\eta = \frac{1}{B^*(1-B^*)}$.

Incorporating these Hessians into equation 49, we obtain:

$$\mathbb{E}_{\hat{B}_k} L_\xi (\hat{B}_k (\xi)) \approx L(B^*) - \frac{1}{8k} \text{Tr} \begin{bmatrix} 2 & 2 \\ 2 & 2 \end{bmatrix} = L(B^*) - \frac{1}{2k}, \quad (51)$$

$$\mathbb{E}_{\hat{B}_k} L_\mu (\hat{B}_k (\mu)) \approx L(B^*) - \frac{1}{2k} \text{Tr} \begin{bmatrix} 1 & 0 \\ 0 & 1 \end{bmatrix} = L(B^*) - \frac{1}{k}. \quad (52)$$

O. Cross decoding matrices and example latents for LFADS AND STNDT

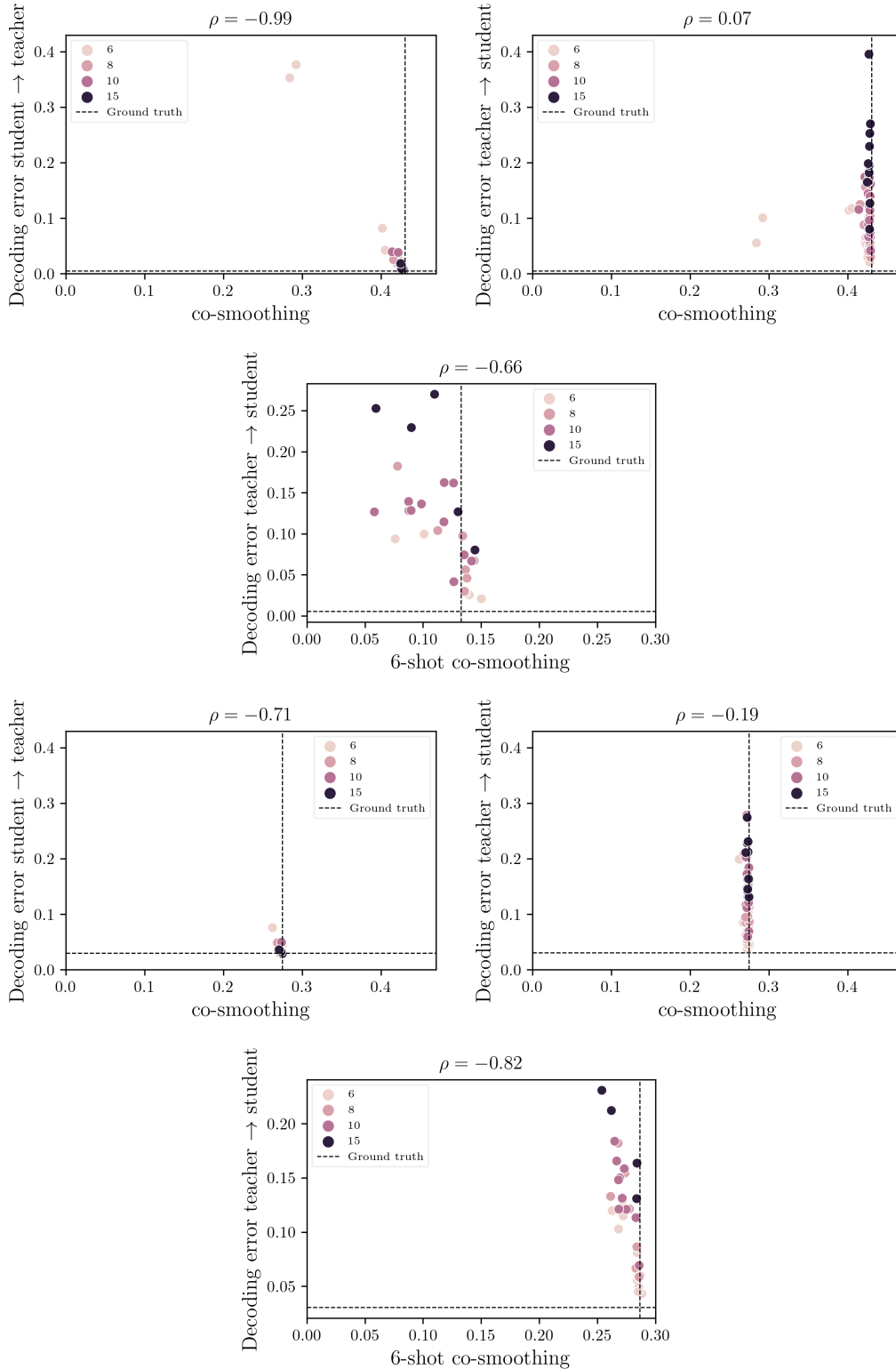


Figure 7. Making co-smoothing harder does not discriminate between models. **Top three:** Increasing the number of held out neurons from $N^{\text{out}} = 50$ to $N^{\text{out}} = 100$. First two panels: Same as main text Fig. 1CD. Lower panel: Same as main text Fig. 4B. **Bottom three:** Decreasing the number of held-in and held-out neurons to $N^{\text{in}} = 5$, $N^{\text{out}} = 5$, $N^{\text{k-out}} = 50$. Panels as in top row. The score does decrease because the problem is harder, but co-smoothing is still not indicative of good models while few-shot is.

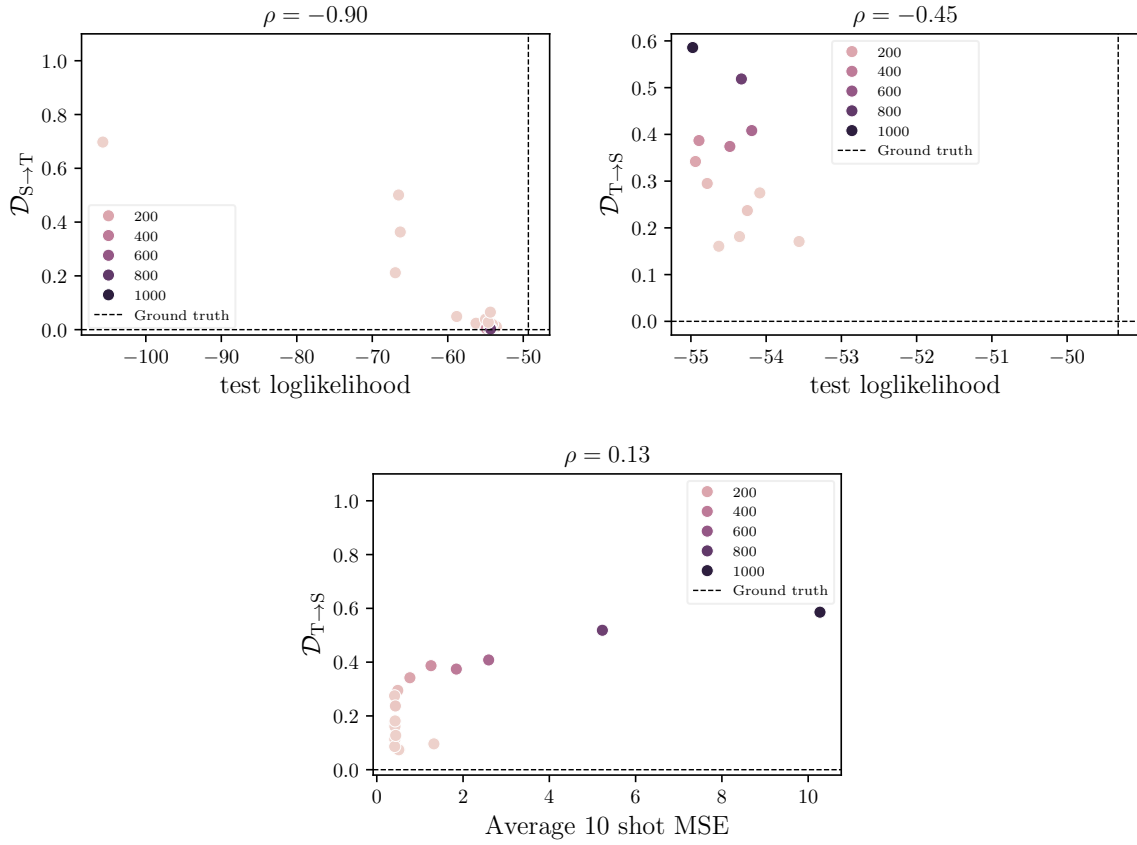


Figure 8. **Left to right:** Student-teacher results for Linear Gaussian State Space Models. We report loglikelihood instead of co-smoothing, and k -shot MSE instead of k -shot co-smoothing.

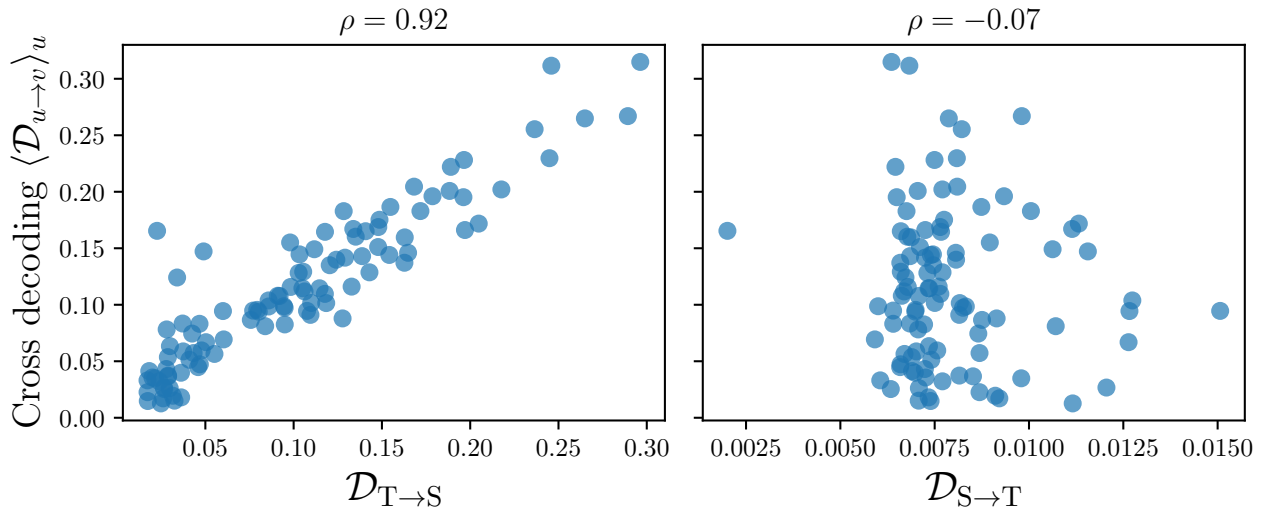


Figure 9. For HMM students with high co-smoothing $\mathcal{Q}_S > \mathcal{Q}_T - 10^{-3}$ (and therefore low $\mathcal{D}_{S \rightarrow T}$ 1D), the cross-decoding metric $\langle \mathcal{D}_{u \rightarrow v} \rangle_{u \in \text{students}}$ is correlated to ground truth distance $\mathcal{D}_{T \rightarrow S}$ and uncorrelated to $\mathcal{D}_{S \rightarrow T}$.

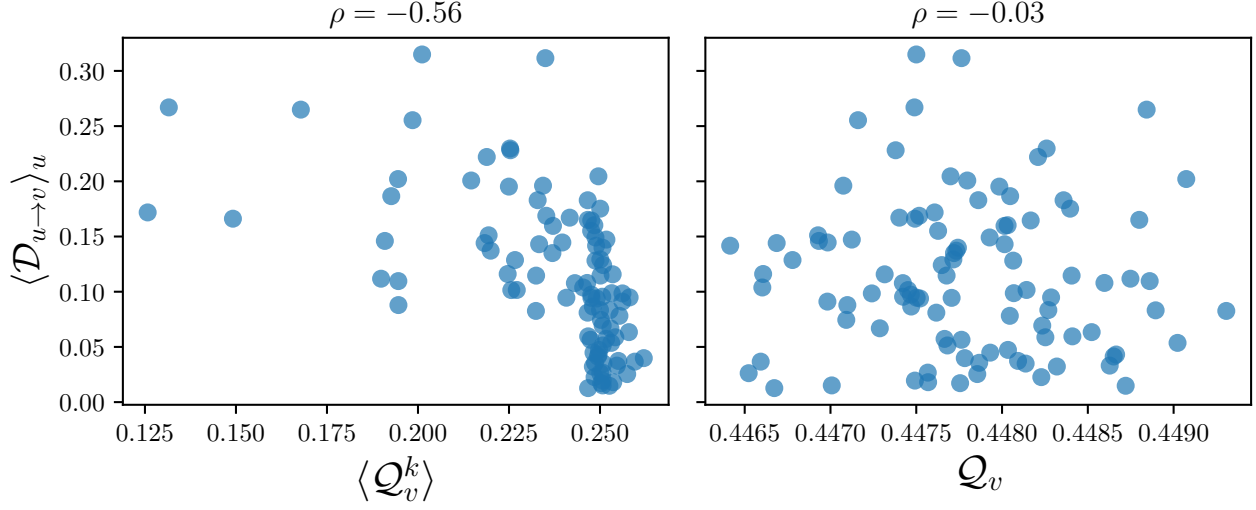


Figure 10. Few-shot co-smoothing validated with cross-decoding in HMMs: a repeat of main text Fig. 6, now in the HMM setting. For HMMs, $v \in$ students, with near-optimal co-smoothing, $Q_v > Q_T - 10^{-3}$, few-shot co-smoothing scores $\langle Q_v^k \rangle$, with $k = 6$, negatively correlate with the cross-decoding metric $\langle \mathcal{D}_{u \rightarrow v} \rangle_u$, used as proxy for the distance from ground truth metric $\mathcal{D}_{T \rightarrow S}$. Meanwhile, co-smoothing scores Q are uncorrelated with the same.

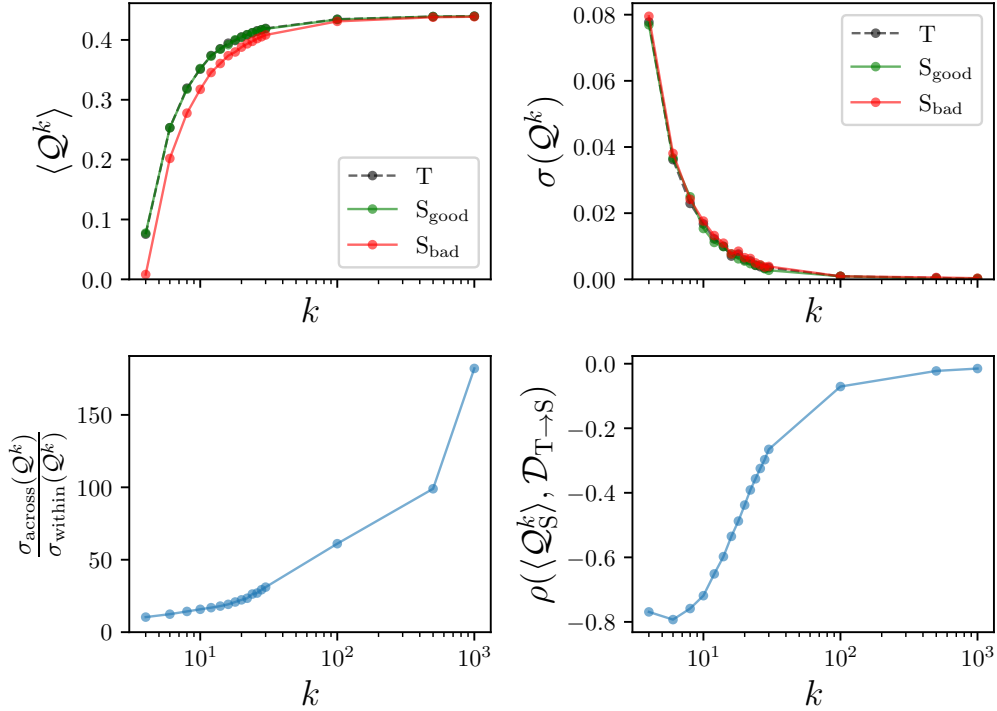


Figure 11. Choosing k and s : analysis with HMMs. **Top-left**: Average k -shot co-smoothing as a function of k for three models, the teacher T, a good and a bad student as (see 2). **Top-right** Standard deviation of k -shot co-smoothing values across resamples. **Bottom-left** Signal to noise ratio, ratio of standard deviation of k -shot co-smoothing values across models vs with models. **Bottom-right**: Pearson's correlation of average k -shot score and the ground-truth decoding measure, for models with high co-smoothing Q , as reported in Fig. 4B for $k = 6$. Here we take $s := \lfloor \frac{S_{\text{train}}}{k} \rfloor$.

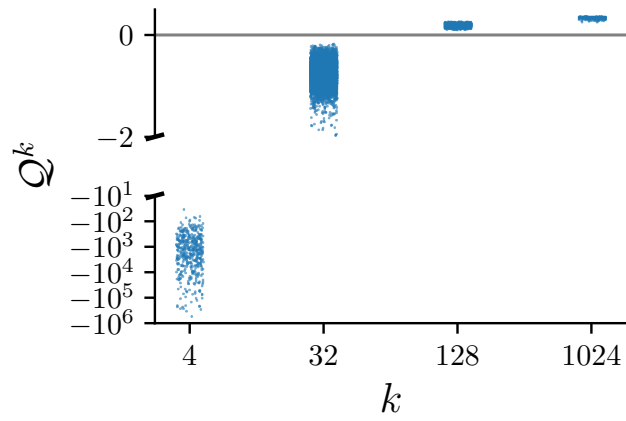


Figure 12. k -shot scores (without averaging over s resamples) for LFADS models on the `mc_maze_20` dataset, as a function of k . $Q^k = 0$ is a baseline score obtained by reporting the mean firing rate for each neuron. For small k scores fall below 0 and become highly variable.

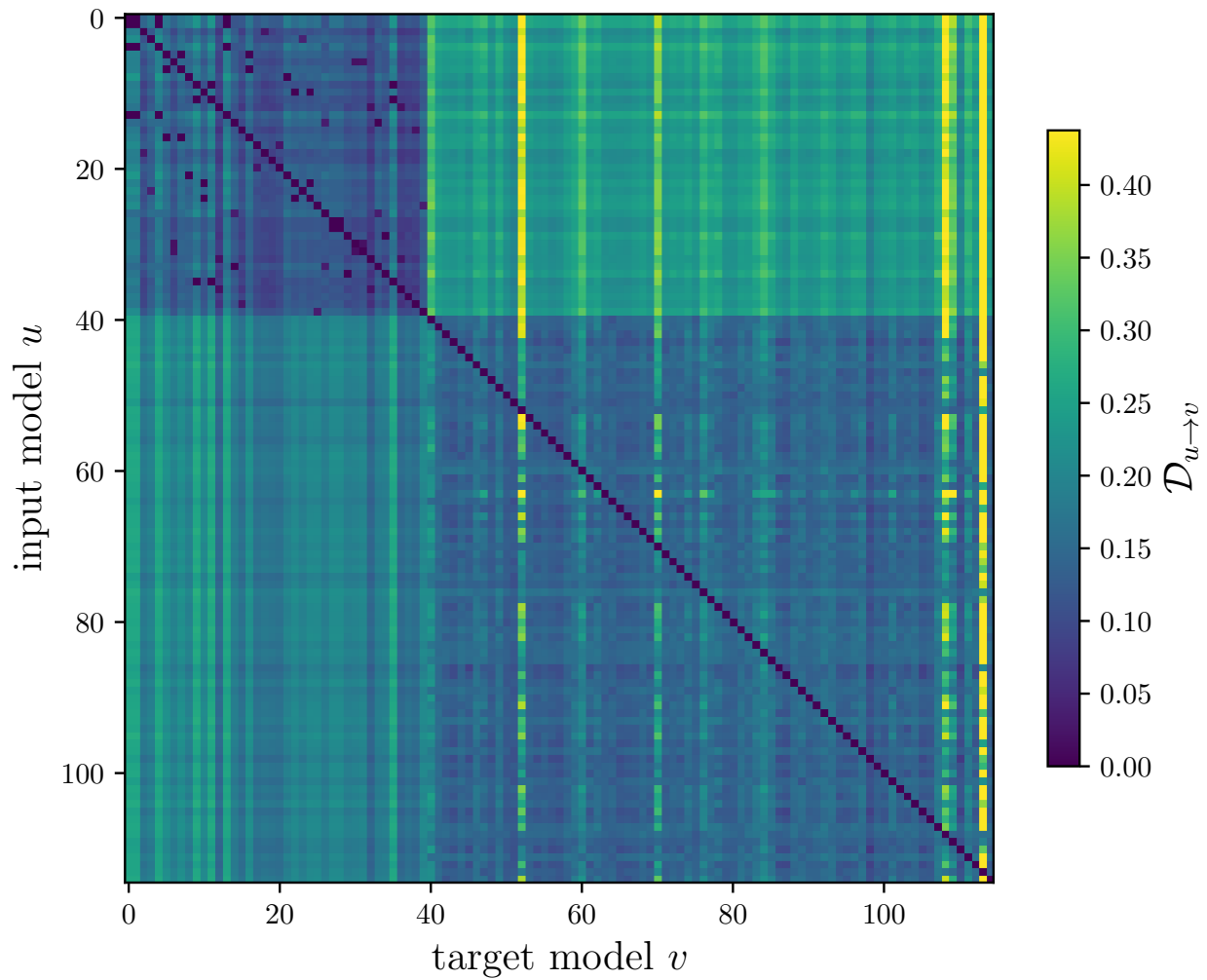


Figure 13. Cross decoding matrix $\mathcal{D}_{u \rightarrow v}$ for all model pairs (u, v) from the combined set of 75 LFADS and 40 STNDT models on mc_maze_20 with near-SOTA co-smoothing $0.345 < \mathcal{Q} < 0.36$. The colourmap saturates at the upper 99% quantile of scores in the matrix to better visualise the bulk of the data.

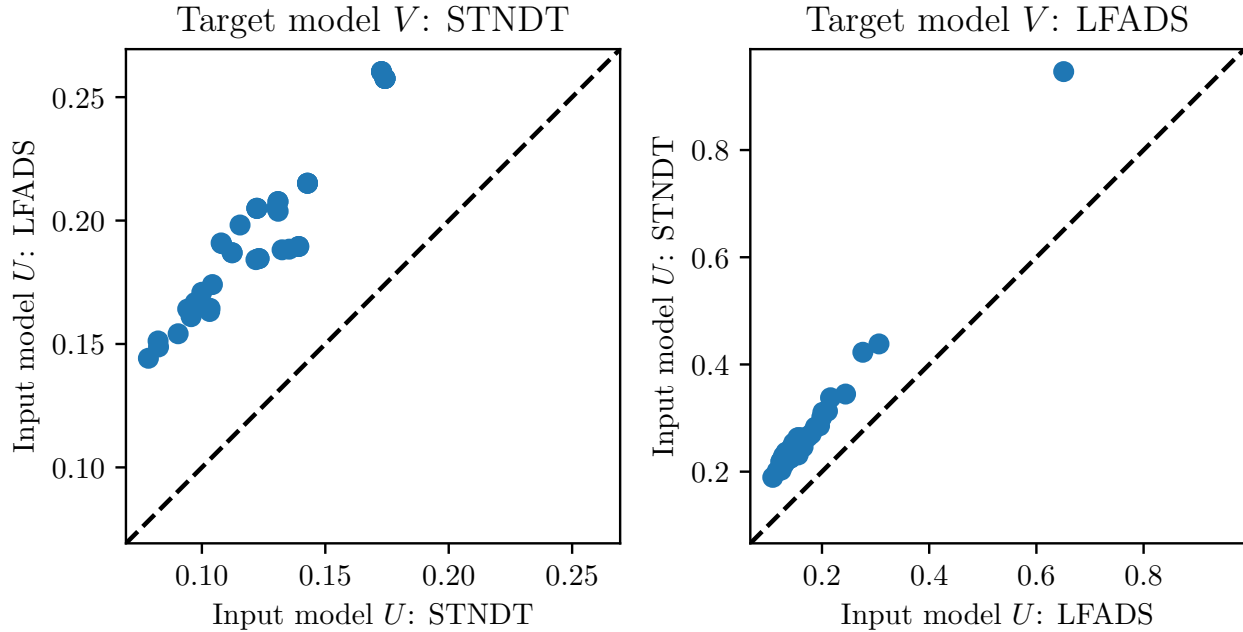


Figure 14. Architecture-wise column means of the cross-decoding matrix. Compare their cross-decoding column means for input models from models of the same architecture versus models of a different architectures, i.e., $\langle \mathcal{D}_{u \rightarrow v} \rangle_{u \in U \setminus \{v\}}$ for target models $v \in V$. LEFT: V is the population of STNDT models and RIGHT: LFADS. All models in $U \cup V$ have near-SOTA co-smoothing, in the range $0.345 < \mathcal{Q} < 0.36$. We do not include the self-decoding scores $\mathcal{D}_{u \rightarrow u}$ as these are trivially near-zero and bias the results.

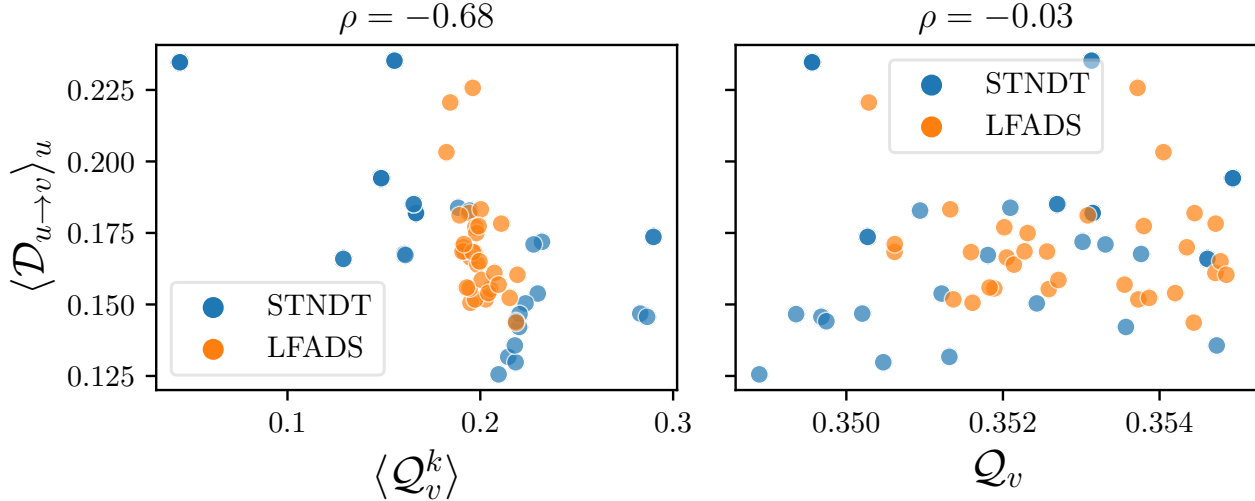


Figure 15. Few-shot scores correlate with the proxy of distance to the ground truth, even in a mixed population of architectures. We repeat the analysis in main text Fig. 6, pooling together the STNDT and LFADS models with high co-smoothing scores $\mathcal{Q} > 0.348$ and compute cross-decoding $\langle \mathcal{D}_{u \rightarrow v} \rangle_u$ for the combined population. To replicate the main text result, we plot models in narrow \mathcal{Q} range, i.e., an upper co-smoothing limit of $\mathcal{Q} < 0.355$, while ensuring that models of both architectures are included.

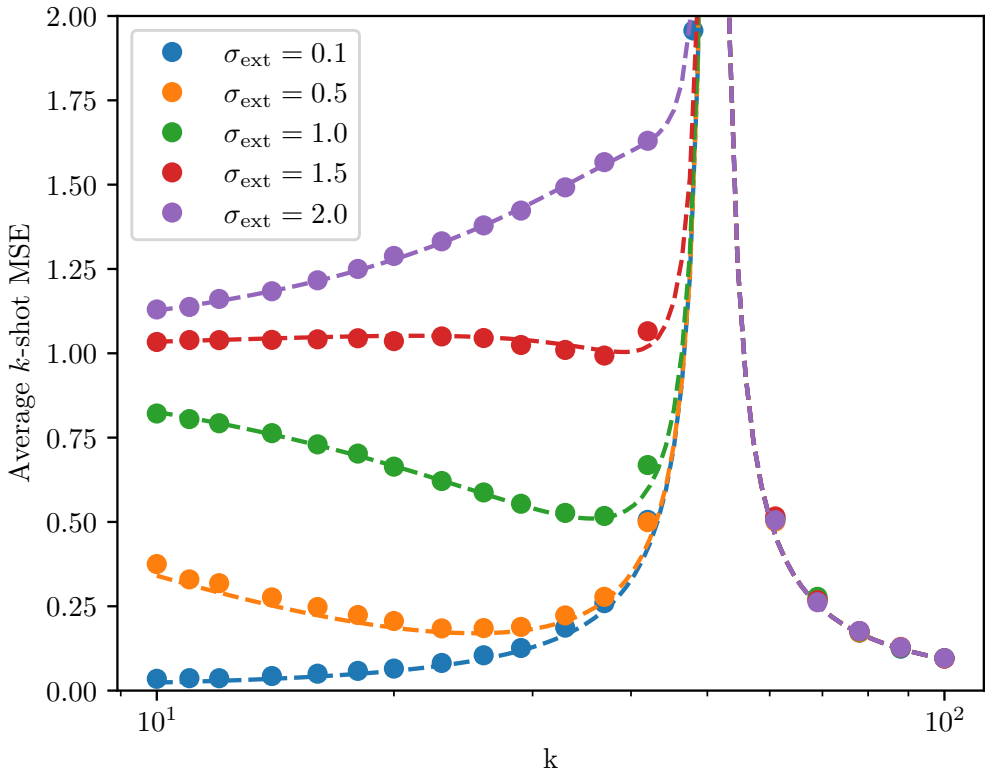
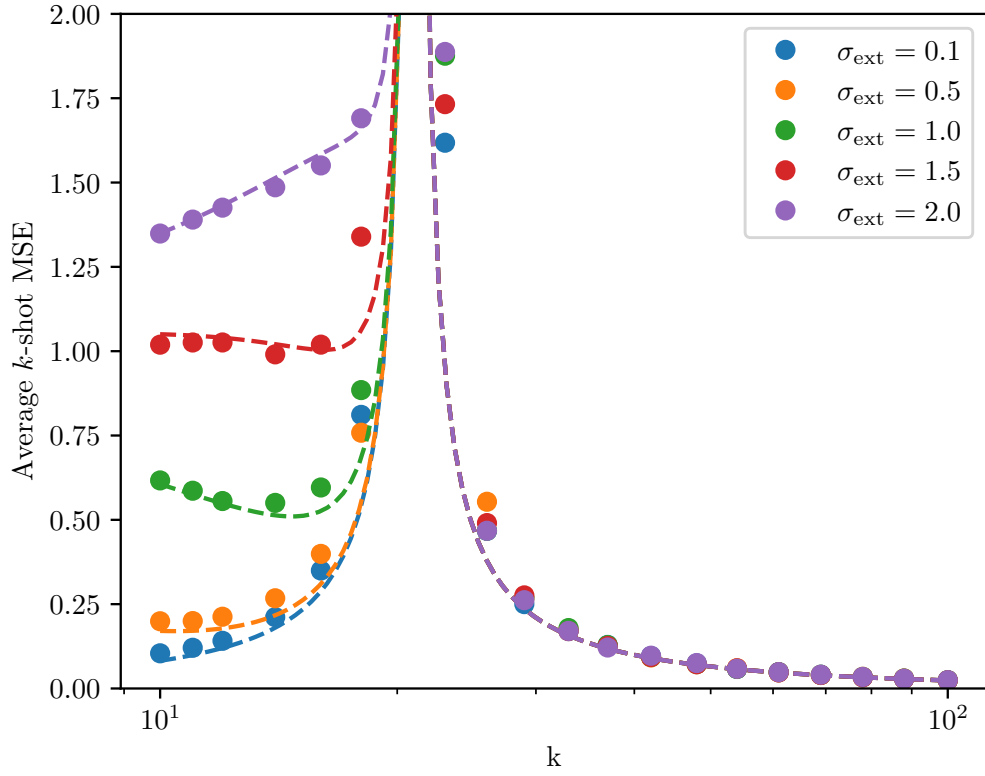


Figure 16. Theoretical analysis of few-shot ridgeless least squares regression for $p = 21$ and $p = 51$. Dots are from numerically solved regressions for finite k and p , and dashed lines are the theoretical predictions from the claims 1 and 2, based on (Hastie et al., 2022).

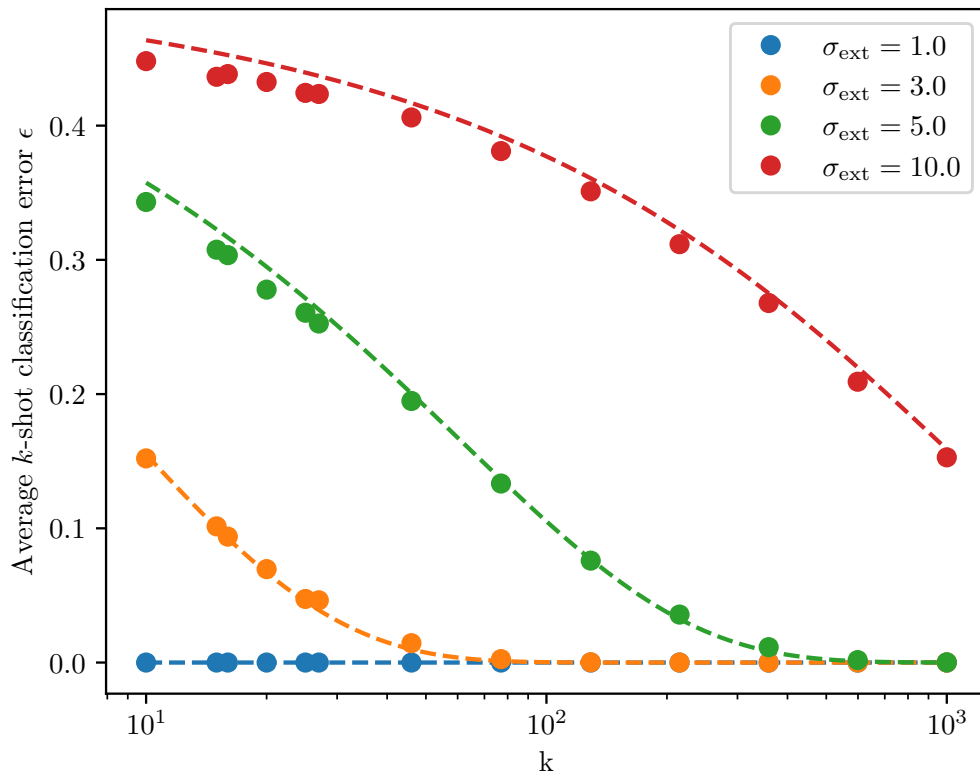


Figure 17. Theoretical analysis of few-shot binary classification with prototype learning with $M = 20$. Dots are numerically computed errors and dashed lines are the theoretical predictions from equation 39, based on (Sorscher et al., 2022).

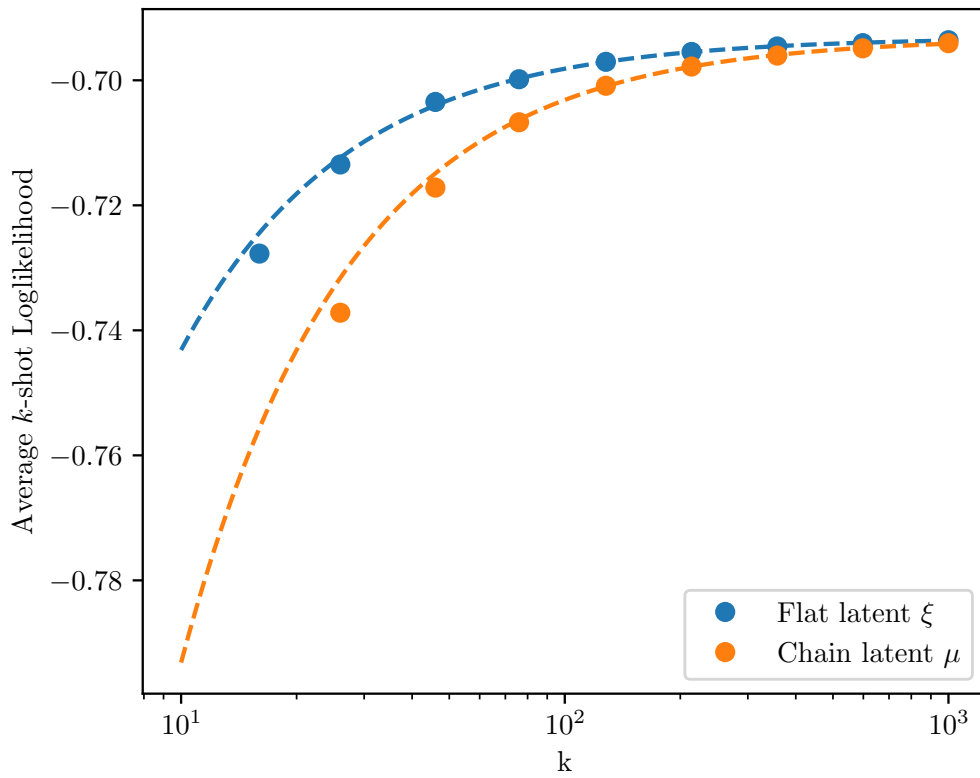


Figure 18. Test loglikelihood, k -shot binomial regression for two, 2-state model latents: a compact latent ξ and an extraneous latent μ . Dots are numerical and dashed lines are theory.

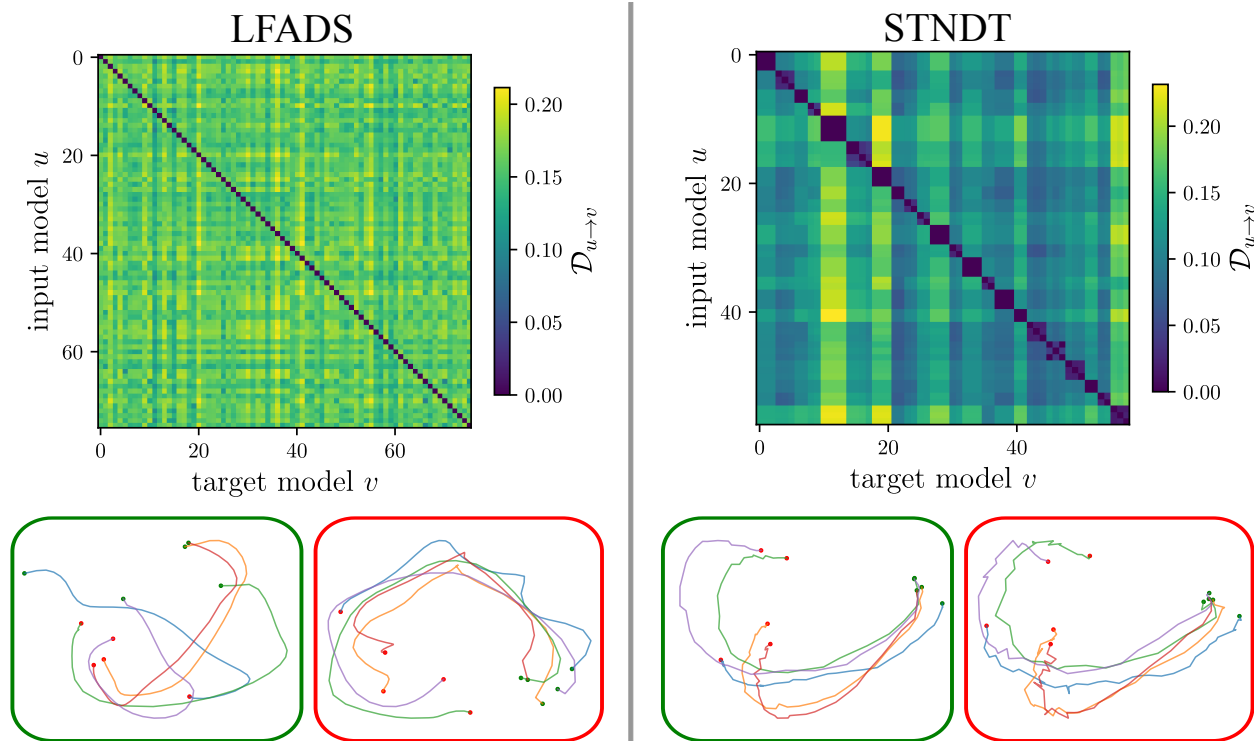


Figure 19. Cross-decoding as a proxy for distance to the ground truth in near-SOTA models. 200 LFADS models (left) and 120 STNDT models (right) were trained on the `mc_maze_20` dataset then selected for high-cosmoothing (appendix F). The latents of each pair of models were decoded from one another, and the decoding error is shown in the matrices. Good models are expected to be decoded from all other models, and hence have low values in their corresponding columns. **Bottom left:** Trajectories of two LFADS models, with the lowest (left and in a green box, best model:= $\operatorname{argmin}_v \langle \mathcal{D}_{u \rightarrow v} \rangle_u$) and highest (right and in the red box, the worst model:= $\operatorname{argmax}_v \langle \mathcal{D}_{u \rightarrow v} \rangle_u$) column averaged cross-decoding errors, projected onto their leading two principal components. Scores for these models are indicated in Fig. 6 by the arrows. Each trace is the trajectory for a single trial, starting at a green dot and ending at a red dot. **Bottom right** Same for STNDT.